ChemPhysChem

Research Article
doi.org/10.1002/cphc.202300511

Chemistry Europe
European Chemical Societies Publishing

www.chemphyschem.org

Special Collection

Effects of Intra-Base Pair Proton Transfer on Dissociation and Singlet Oxygenation of 9-Methyl-8-Oxoguanine—1-Methyl-Cytosine Base-Pair Radical Cations

May Myat Moe,[a, b] Midas Tsai,[c] and Jianbo Liu*[a, b]

8-Oxoguanosine is the most common oxidatively generated base damage and pairs with complementary cytidine within duplex DNA. The 8-oxoguanosine—cytidine lesion, if not recognized and removed, not only leads to G-to-T transversion mutations but renders the base pair being more vulnerable to the ionizing radiation and singlet oxygen ($^1O_2$) damage. Herein, reaction dynamics of a prototype Watson—Crick base pair $[9MOG\cdot1MC]^{\bullet+}$, consisting of 9-methyl-8-oxoguanine radical cation ($9MOG^{\bullet+}$) and 1-methylcytosine (1MC), was examined using mass spectrometry coupled with electrospray ionization. We first detected base-pair dissociation in collisions with the Xe gas, which provided insight into intra-base pair proton transfer of $9MOG^{\bullet+}\cdot1MC \rightleftharpoons [9MOG - H_{N1}]^{\bullet}\cdot[1MC + H_{N3'}]^{+}$ and subsequent non-statistical base-pair separation. We then measured the reaction of $[9MOG\cdot1MC]^{\bullet+}$ with $^1O_2$, revealing the two most probable pathways, C5-O_2 addition and H_{N7}-abstraction at 9MOG. Reactions were entangled with the two forms of 9MOG radicals and base-pair structures as well as multi-configurations between open-shell radicals and $^1O_2$ (that has a mixed singlet/triplet character). These were disentangled by utilizing approximately spin-projected density functional theory, coupled-cluster theory and multi-referential electronic structure modeling. The work delineated base-pair structural context effects and determined relative reactivity toward $^1O_2$ as $[9MOG - H]^{\bullet} > 9MOG^{\bullet+} > [9MOG - H_{N1}]^{\bullet}\cdot[1MC + H_{N3'}]^{+} \geq 9MOG^{\bullet+}\cdot1MC$.

1. Introduction

Oxidatively generated DNA damage upon the attack of various exogenous and endogenous oxidants introduces a variety of deleterious processes including mutagenesis and cancer.[1] Among the different components of DNA, the guanine nucleobase is the most readily oxidizable due to its lower ionization potential (IP = 7.68 eV in the gas phase[2] and 4.42 eV in aqueous[3]) and lower oxidation potential (E° = 1.29 V vs NHE)[4] compared to all the other natural DNA nucleobases, phosphate and sugar moiety (See IP and E° of DNA components in Table S1 in the Supporting Information). Oxidation of guanine nucleobase and guanosine nucleoside may occur via a Type I mechanism[5] mediated by one-electron oxidants such as $^{\bullet}OH$ and $O_2^{\bullet-}$ or a Type II mechanism[5c–f,h,6] mediated by the lowest electronically excited singlet molecular oxygen O_2 [$a^1\Delta_g$].[7] The Type I oxidation of guanine/guanosine (hereafter refer to G) leads to several products including 8-oxoguanosine (OG),[5a,g,8] 2,5-diaminoimidazolone (Iz),[8–9] 2,2,4-triamino-2*H*-oxazol-5-one (Oz) (in equilibrium with guanidinooxalamide),[5a,8–10] and 2,6-diamino-4-hydroxy-5-formamidopyrimidine (FapyG).[5a,g,8,11] The type II oxidation of guanosine is structural and condition dependent: the reaction leads to OG as a main product within DNA[12] whereas forms spiroiminodihydantoin (Sp, under basic condition)[13] and guanidinohydantoin (Gh, under acidic condition) in free nucleobases/nucleosides and short oligonucleosides.[14]

As the most common base damage found in cells, OG becomes more prone to further oxidatively generated damage due to its 0.75 eV lower IP (6.93 eV in the gas phase)[15] and 0.55 V lower E° (0.74 V vs NHE)[16] than those of G. The reactivity of OG toward $^1O_2$ is about two orders of magnitude higher than that of G.[17] These facts have struck extensive research interests and many laboratories have contributed to the work in delineating primary and secondary $^1O_2$ oxidation mechanisms of OG.[14a,17b,18] Scheme S1 in the Supporting Information outlines major reaction pathways and products for the $^1O_2$ oxidation of OG. In brief, the $^1O_2$ oxidation of a neutral, isolated OG starts with a [2 + 2]-cycloaddition.[18a] The product 4,5-dioxetane is stable only at low temperature and decomposes upon warming.[18a] One decomposition pathway is via the cleavage of both C4–C5 and O–O bonds, which leads to the formation of a transient 9-membered macrocycle,[18a,c] followed by hydrolysis and decarboxylation to cyanuric acid and urea.[18a,c] Another decomposition pathway of 4,5-dioxetane leads to the formation of a hydroperoxide 5-OOH-OG.[18h]

[a] M. M. Moe, Prof. Dr. J. Liu
Department of Chemistry and Biochemistry
Queens College of the City University of New York
65-30 Kissena Blvd., Queens, NY 11367, USA
E-mail: jianbo.liu@qc.cuny.edu

[b] M. M. Moe, Prof. Dr. J. Liu
Ph.D. Program in Chemistry
The Graduate Center of the City University of New York
365 5th Ave., New York, NY 10016, USA

[c] Prof. Dr. M. Tsai
Department of Natural Sciences
LaGuardia Community College
31-10 Thomson Ave., Long Island City, NY 11101, USA

Supporting information for this article is available on the WWW under https://doi.org/10.1002/cphc.202300511

Special Collection An invited contribution to a Special Collection on Physical Chemistry of Nucleic Acid Damage and Photomedicine

The latter presents a wide range of downstream conversions depending on reaction conditions. The reduction of 5-OOH-OG give rises to 5-hydroxyl-OG[18a,h] which transforms to Sp at pH $\geq$ 7[14a,17b,18h,j] or Gh at pH $\leq$ 7.[14a,18j] Alternatively, the C5–C6 cleavage of 5-OOH-OG and concurrent decarboxylation lead to dehydro-guanidinohydantoin (Gh^{OX}).[18f] Gh^{OX} further evolves to Iz and Oz[17b,18b] as well as ring-opened guanidinooxalamide.[18d,e,i] The literature results demonstrate the variability and versatility of the $^1O_2$ chemistry with OG and their sharp dependence on reactant structures and reaction conditions. Particularly, the oxidation of OG within DNA differs from that of an isolated monomer. For example, the Gh^{OX} intermediate within DNA or oligonucleotides undergoes hydration at the N3–C4 double bond, leading to parabanic acid (Pa) after release of guanidine and to oxaluric acid (Oxa) after further hydrolysis.[17b,18f,g]

Moreover, the gas-phase experiment carried out in our laboratory revealed that an isolated protonated $[OG+H]^+$ is not prone to the $^1O_2$ oxidation at all whereas the isolated deprotonated $[OG-H]^-$ forms $[5\text{-}OOH_{N7}\text{-}OG-H]^-$(wherein the subscript indicates the original position of proton) and $[dioxetane-H]^-$ in the $^1O_2$ oxidation.[18k] Gas-phase reactions occurred in a rarefied environment in the absence of solvents, counterions and other solution variables (such as pH, temperature, dielectric constant, etc.). This allows for detection of intrinsic OG reactivity toward $^1O_2$ and the early-stage reaction kinetics and dynamics, all of which forms a basis to understand and predict the divergent downstream pathways and secondary conversions observed in aqueous solution. In view of a glaring lack of such information in the literature, more gas-phase reaction studies are warranted on the DNA nucleobase and nucleoside oxidation chemistry as a supplementary to conventional solution-phase experiments.

More recently, our laboratory investigated the $^1O_2$ reactions with the radical cations of 8-oxoguanosine ($OG^{\bullet+}$) and its model compound 9-methyl-8-oxoguanine ($9MOG^{\bullet+}$, wherein the methyl group mimics a ribose sugar) in the gas phase and identified C5-O_2 adducts as the initial oxidation products.[18l] That work, for the first time, provided the correlated information of nucleobase ionization and singlet oxygenation. Yet, we had a dilemma when extrapolating the gas-phase chemistry of $OG^{\bullet+}$ into aqueous solution. An isolated $OG^{\bullet+}$ or that within single-stranded (*ss*) DNA has a pK_a of 3.42 for the N1–H.[16b] Consequently, $OG^{\bullet+}$ would immediately lose a proton to water and form a conjugated $[OG-H]^{\bullet}$ neutral radical. The scenario, however, changes in double-stranded (*ds*) DNA, wherein OG takes place of G in pairing with C (cytidine) in a Watson–Crick (WC) base pair.[19] Note that OG may also form a Hoogsteen (HG) base pair with C;[20] nevertheless, this was not found in duplex DNA.[19–20] According to our calculations (see Supporting Information), the HG-$[OG{\cdot}C]^{\bullet+}$ conformers have much higher energies than their WC counterparts and are negligible. Within the WC-$OG^{\bullet+}{\cdot}C$ base pair, $OG^{\bullet+}$ shares its N1–H with the N3′ (pK_a 4.58) of C,[21] effectively trapping the acidic proton within the base pair even in aqueous solution. In that sense, the work of $OG^{\bullet+}$ and $[OG-H]^{\bullet}$ in the gas phase has provided a basic knowledge of DNA radicals, but the study of gas-phase $[OG{\cdot}C]^{\bullet+}$ would be more appropriate to characterize chemistry in oxidized DNA and provide more biologically relevant information including effects of structural context. Therefore, this work investigated reaction of $^1O_2$ with a model WC-$[OG{\cdot}C]^{\bullet+}$ system consisting of 9-methyl-8-oxoguanine ($9MOG^{\bullet+}$) and 1-methyl-cytosine (*i.e.*, $[9MOG{\cdot}1MC]^{\bullet+}$).

The Burrows group reported the formation and oxidation of $[OG{\cdot}C]^{\bullet+}$ by oxidizing OG·C with one-electron oxidants ($ONOOCO_2^-$-derived $CO_3^{\bullet-}/{}^{\bullet}NO_2$ and Na_2IrCl_6) in solution.[22] They measured the relative reactivity toward one-electron oxidation as $OG^{\bullet+}$ nucleoside $\geq$ $OG^{\bullet+}$ in *ss* oligonucleosides > $[OG{\cdot}C]^{\bullet+}$ and provided valuable information on how the structural context (electrostatic, base stacking, base pairing, sequence) affects the partitioning of the key intermediate 5-OH-OG along the two hydantoin pathways leading to Sp and Gh, respectively.[22] However, to the best of our knowledge, no study has been reported on the $^1O_2$ oxidation of $[OG{\cdot}C]^{\bullet+}$.

Base pairing is essential to maintaining the integrity of DNA for cellular activities. A unique reaction related to base pairing in duplex DNA is the intra-base pair proton transfer (PT) via H-bonds, for example, $9MOG^{\bullet+}{\cdot}1MC$ (referred to as a conventional conformer) $\rightleftharpoons$ $[9MOG-H_{N1}]^{\bullet}{\cdot}[1MC+H_{N3'}]^+$ (a PT conformer). The PT equilibrium and kinetics may be revealed by measuring collision-induced dissociation (CID) of the base-pair ions, as each type of base-pair conformer produces distinctly different fragment ions. The CID results can provide insight into the unique chemical environment of bases in duplex DNA that is expected to influence the singlet oxygenation reaction of base pair versus that of an isolated monomeric nucleoside.

The remainder of the paper is organized as follows. In the Results and Discussion, we first report the CID results of $[9MOG{\cdot}1MC]^{\bullet+}$ followed by the analysis of dissociation potential energy diagram, intra-base pair PT and dissociation kinetics. We then proceed to the experimental measurement and theoretical modeling of the $^1O_2$ reaction with $[9MOG{\cdot}1MC]^{\bullet+}$, including comparisons with the oxidation results of an isolated $9MOG^{\bullet+}$ and $[9MOG-H]^{\bullet}$. The effects of structural context on base-pair singlet oxygenation reactions as well as the biological implications are summarized in Conclusions. At last, in the Experimental and Computational Section, experimental techniques, quantum chemistry computational methods and kinetics modeling are elaborated.

2. Results and Discussion

2.1. Assessment of $[9MOG{\cdot}1MC]^{\bullet+}$ Structures

2.1.1. Base-Pair Conformers

$[9MOG{\cdot}1MC]^{\bullet+}$ has various conformers and tautomers due to the keto-enol and amino-imine isomerization, intra-base pair PT and hydrogen transfer (HT), as well as WC and HG pairing structures. A total of 10 conformers were identified for $[9MOG{\cdot}1MC]^{\bullet+}$ within an energy range of 2.1 eV using the

ωB97XD/6-311++G(d,p) level of theory. Their structures, relative enthalpies (ΔH at 298 K, with respect to the global minimum), base-pairing energies and thermal equilibrium populations are provided in Scheme S2 in the Supporting Information. Their Cartesian coordinates are also provided in the Supporting Information. Four of these conformers belong to WC structures and the remaining six are HG. Within each group, the conformers are listed in the order of relative enthalpies as indicated by sequential numbers. A structural formula is provided for each conformer, and the complementary pair of PT and HT isomers are indicated in parentheses.

The global minimum WC structure, WC-[9MOG·1MC]$^{\bullet+}$_1, adopts a conventional structure in that the N1–H of 9MOG remains covalently bonded to 9MOG. The second lowest-energy WC conformer, WC-[9MOG·1MC]$^{\bullet+}$_2, with the energy of 0.01 eV above the global minimum, has the N1–H of 9MOG shifted to the N3′ of 1MC and thus represents a PT conformer WC-[9MOG − H_{N1}]$^{\bullet}$·[1MC+$H_{N3'}$]$^{+}$. The other two WC conformers adopt an enol conformation and both are 0.8–1.0 eV higher in energy than WC-[9MOG·1MC]$^{\bullet+}$_1. The thermal equilibrium populations of WC-[9MOG·1MC]$^{\bullet+}$_1 and _2 are 62% and 38%, respectively. The two of them are expected to account for all of the WC structures in the ion beam. The other WC structures are unlikely to populate under the experimental condition.

Compared to WC-[9MOG·1MC]$^{\bullet+}$_1, the major HG structures, HG-[9MOG − H_{N7}]$^{\bullet}$·[1MC+$H_{N3'}$]$^{+}$_1 and _2, lie in energy 0.26–0.31 eV higher and have base-pairing energy 0.3–0.4 eV less. More importantly, no HG structure was found for OG·C in duplex DNA.[19–20] Therefore, we chose to use WC-[9MOG·1MC]$^{\bullet+}$_1 and _2 as starting reactant ion structures in the analysis of experimental results. Our assignments are consistent with the previous study[23] and have been further validated by the base-pair dissociation threshold measurements in the present work (which ruled out base-pair structures with binding energy less than 1.8 eV). In the remaining sections, we refer the two lowest-energy WC base-pair structures as 9MOG$^{\bullet+}$·1MC and [9MOG − H_{N1}]$^{\bullet}$·[1MC+$H_{N3'}$]$^{+}$ and their mixtures as [9MOG·1MC]$^{\bullet+}$.

As shown in Scheme 1, the electron configuration of 9MOG$^{\bullet+}$·1MC demonstrates a non-Aufbau principle. The singly occupied molecular orbital (SOMO, localized on 9MOG$^{\bullet+}$) lies in energy below the highest occupied molecular orbital (HOMO, localized on 1MC). On the other hand, [9MOG − H_{N1}]$^{\bullet}$·[1MC+$H_{N3'}$]$^{+}$ restores the expected Aufbau-MO behavior in that the highest doubly occupied molecular orbital (HDMO, localized on [1MC+H]$^{+}$) lies in energy below the SOMO (localized on [9MOG − H_{N1}]$^{\bullet}$). Non-Aufbau[24] MO behavior was also found in [G·C]$^{\bullet+}$[25] and [9MG·1MC]$^{\bullet+}$.[26]

2.1.2. Base-Pair Dissociation Threshold Energies and Product Ion Cross Sections

The CID of [9MOG·1MC]$^{\bullet+}$ with the Xe gas was measured over the center-of-mass collision energy (E_{CM}) range from 0.05 to 5.0 eV. The experiment was performed on a guided-ion beam tandem mass spectrometer.[27] The tandem mass spectrum

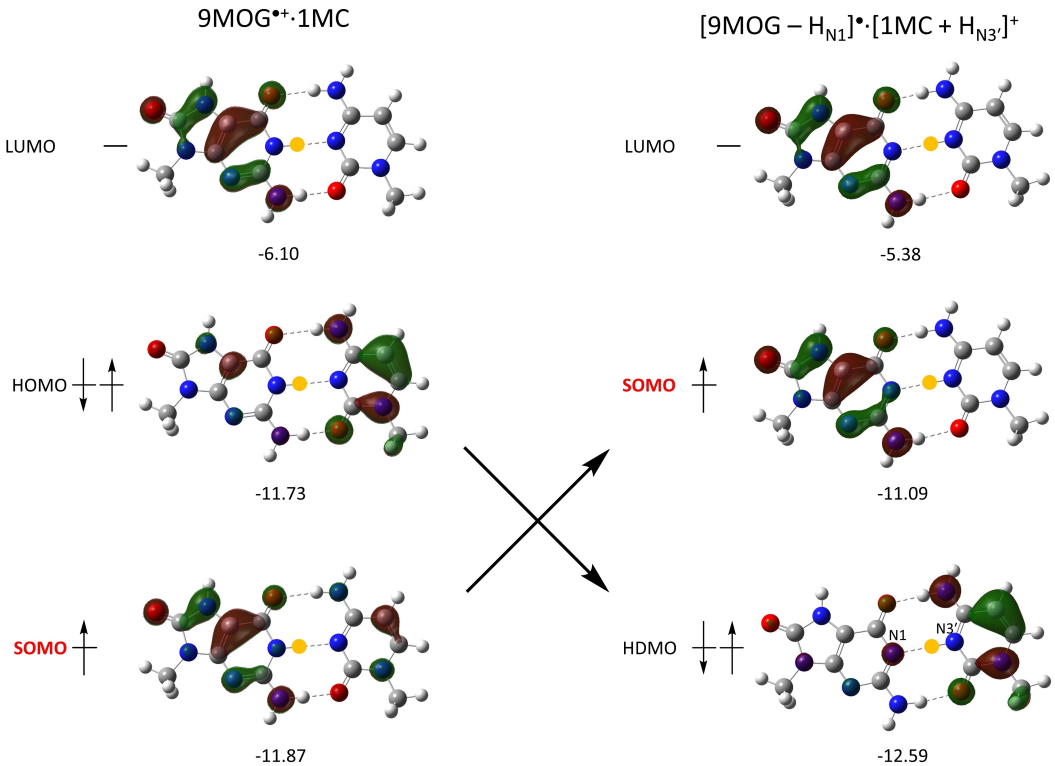

Scheme 1. Frontier MOs of 9MOG$^{\bullet+}$·1MC and [9MOG − H_{N1}]$^{\bullet}$·[1MC+$H_{N3'}$]$^{+}$, with energies (in eV) calculated at ωB97XD/6-311++G(d,p). The proton involved in intra-base pair PT is highlighted in orange.

recorded at $E_{CM}=3$ eV (Figure 1a) serves as a representative product ion mass spectrum. The dissociation product ions include 9MOG$^{\bullet+}$ (*m/z* 181) and $[1MC+H]^+$ (*m/z* 126), verifying the formation of both 9MOG$^{\bullet+}\cdot$1MC and $[9MOG-H_{N1}]^{\bullet}\cdot[1MC+H_{N3'}]^+$ and their respective dissociation. Note that the two conformers have formed not only in the primary ion beam but also in the collisional activation-induced isomerization within the scattering cell. Their 0 K dissociation energies were calculated at the DLPNO-CCSD(T)/aug-cc-pVQZ//ωB97XD/6-311++G(d,p) levels of theory as:

$$9MOG^{\bullet+}\cdot 1MC \rightarrow 9MOG^{\bullet+} + 1MC \quad \Delta H\ (0\ K) = 1.87\ eV \tag{1}$$

$$[9MOG-H_{N1}]^{\bullet}\cdot[1MC+H_{N3'}]^+ \rightarrow [9MOG-H]^{\bullet} + [1MC+H]^+ \quad \Delta H\ (0\ K) = 1.79\ eV \tag{2}$$

Figure 1b presents individual product ion cross sections as a function of kinetic energy both in the center-of-mass (E_{CM}) and laboratory frame (E_{lab}). As the E_{CM} scale directly relates to dissociation threshold energy, it is adopted in the following discussion. The cross section of 9MOG$^{\bullet+}$ rises slowly from $E_{CM}=1$ eV and starts to level off at $E_{CM}=4.2$ eV; the cross section of $[1MC+H]^+$, on the other hand, rises quickly and reaches a plateau around 3 eV before it finally declines at $E_{CM}\geq 4$ eV. $[1MC+H]^+$ dominates in product ions throughout the whole experimental energy range. To extract the 0 K dissociation energy E_0 of each conformer, individual cross sections were analyzed using a modified line-of-center (LOC) model[28] described in the Experimental and Computational Section. The best LOC-fitted cross sections are presented by solid lines, and LOC-fitted E_0 for individual product ion channels are indicated by vertical arrows. The E_0 for reaction (1) [Eq. (1)] was determined to be 1.88 ± 0.1 eV, while that for reaction (2) [Eq. (2)] was determined to be 1.85 ± 0.1 eV. The uncertainty of E_0 was determined by a set of independent LOC fits using a reasonable range of fitting parameters and included the uncertainty in the absolute value of E_{CM}. Overall, the LOC model was able to successfully reproduce the experimental cross sections from energies below the threshold to $E_{CM}=4$–5 eV. The two fitted E_0 values are in good agreement with the calculated ΔH (0 K) for reactions (1) and (2).

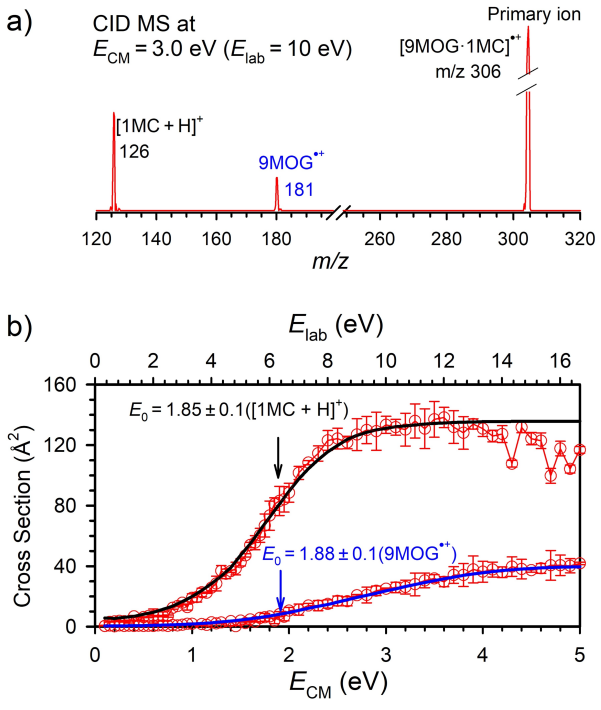

Figure 1. CID of [9MOG·1MC]$^{\bullet+}$ with Xe. a) Product ion mass spectrum recorded at $E_{CM}=3.0$ eV, and b) product ion cross section as a function of kinetic energy in the laboratory frame (E_{lab}, upper x-axis) and center-of-mass frame (E_{CM}, lower x-axis). Red circles with error bars are experimental data and solid lines are LOC fits.

In the CID experiment, the $[9MOG-H_{N1}]^{\bullet}\cdot[1MC+H_{N3'}]^+$ conformer could have originated from the ion source or formed from 9MOG$^{\bullet+}\cdot$1MC upon collisional activation. It was difficult to determine relative contributions. Fortunately, the energy of $[9MOG-H_{N1}]^{\bullet}\cdot[1MC+H_{N3'}]^+$ is only 0.03 eV above 9MOG$^{\bullet+}\cdot$1MC and this amount is within the 0.1 eV experimental uncertainty. In our analysis, all reaction energies are presented with regard to the global minimum 9MOG$^{\bullet+}\cdot$1MC. The LOC fits have also ruled out significant contributions from any high-energy lying base-pair conformers (otherwise, we would have observed inflection in the cross section[29] at a particular E_{CM}). The declining cross section for $[1MC+H]^+$ at higher E_{CM} may be partially due to a competition between the two product channels, and partially due to the difficulty of collecting product ions with increasing radial velocity by the ion guide and Einzel lenses. The cross section for 9MOG$^{\bullet+}$ should have experienced the same issues but was not as severe.

To assess the CID efficiency, hard-sphere collision cross sections ($\sigma_{collision}$) for the two base-pair conformers with Xe were calculated using the orientation-averaged projected area method available in the *IMoS* program.[30] Molecular structures and polarizabilities were acquired from electronic structure calculations at ωB97XD/6-311++G(d,p). The two conformers have the same $\sigma_{collision}$ of 170 Å^2, which matches the sum of 9MOG$^{\bullet+}$ and $[1MC+H]^+$ cross sections at $E_{CM}\geq 4$ eV. It indicates that at high energies every single collision has led to detectable base-pair dissociation.

2.1.3. Comparison of the Experiment with a Statistical Model

Static Potential Energy Diagram for Intra-Base Pair PT and Dissociation. To get insight into base-pair dissociation dynamics, we first examined the schematic reaction coordinate and 0 K potential energy diagram of 9MOG$^{\bullet+}\cdot$1MC and $[9MOG-H_{N1}]^{\bullet}\cdot[1MC+H_{N3'}]^+$ constructed using the DLPNO-CCSD(T)/aug-cc-pVQZ//ωB97XD/6-311++G(d,p) method, as shown in Figure 2. 9MOG$^{\bullet+}\cdot$1MC may transfer the N1–H of 9MOG to the N3′ of 1MC, yielding $[9MOG-H_{N1}]^{\bullet}\cdot[1MC+H_{N3'}]^+$. The PT barrier, TS-PT, lies in energy 0.11 eV above 9MOG$^{\bullet+}\cdot$1MC and 0.08 eV above $[9MOG-H_{N1}]^{\bullet}\cdot[1MC+H_{N3'}]^+$. Since this barrier height is comparable to thermal energy ($kT=0.03$ eV) and much lower than the dissociation energies, a thermal equilibrium could be

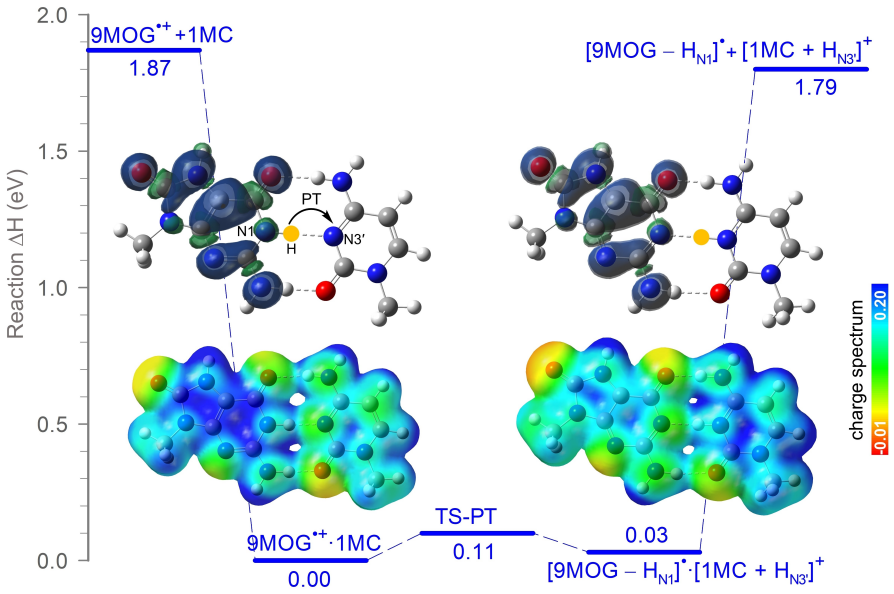

Figure 2. Schematic reaction coordinate and potential energy diagram of $9MOG^{\bullet+}\cdot 1MC$ and $[9MOG - H_{N1}]^{\bullet}\cdot[1MC+H_{N3'}]^{+}$ calculated at 0 K using the DLPNO-CCSD(T)/aug-cc-pVQZ//ωB97XD/6-311++G(d,p) levels of theory. Insets show the base-pair spin density contours and electrostatic potential maps (ESP, with the color bar for charge scale) wherein C, H, O and N atoms are in gray, white, red and blues colors, respectively. The proton involved in PT is highlighted in orange.

expected between the two conformers. $9MOG^{\bullet+}\cdot 1MC$ and $[9MOG - H_{N1}]^{\bullet}\cdot[1MC+H_{N3'}]^{+}$ dissociate to $9MOG^{\bullet+}+1MC$ (calculated $\Delta H = 1.87$ eV and experimental $E_0 = 1.88 \pm 0.1$ eV) and $[9MOG - H_{N1}]^{\bullet}+[1MC+H_{N3'}]^{+}$ (calculated $\Delta H = 1.79$ eV and experimental $E_0 = 1.85 \pm 0.1$ eV), respectively.

The insets in Figure 2 illustrate the spin density contour plots (top) and electrostatic potential-fitted maps (ESP, bottom) for the two base-pair conformers. The ESP maps provide a visualization of charge distribution. In the $9MOG^{\bullet+}\cdot 1MC$ conformer, the 9MOG moiety carries most of the positive charge as indicated by the color scheme. Following PT, the 9MOG moiety in $[9MOG - H_{N1}]^{\bullet}\cdot[1MC+H_{N3'}]^{+}$ loses charge to the 1MC moiety, and the latter has overall more positive charge than 9MOG, albeit the charge is quite diffused over 1MC. The spin density plots indicate the location of the radical electron. In both conformers, the unpaired electron is exclusively located on 9MOG. In this sense, charge and spin are separated in $[9MOG - H_{N1}]^{\bullet}\cdot[1MC+H_{N3'}]^{+}$.

Product Ratios. The experimentally determined product ion ratio of $\frac{[1MC+H]^{+}}{9MOG^{\bullet+}}$ is plotted in Figure 3 as a function of E_{CM}. The ratio is up to 7.3 at $E_{CM} = 2.5$–2.6 eV, drops to 6 at 2.7–2.8 eV, 5 at 2.9–3.3 eV, 4 at 3.4–4.4 eV, and maintains around 3 throughout 5 eV. The product ratio implies that either the population of $[9MOG - H_{N1}]^{\bullet}\cdot[1MC+H_{N3'}]^{+}$ exceeded that of $9MOG^{\bullet+}\cdot 1MC$ upon collisional activation, or the dissociation rate of $[9MOG - H_{N1}]^{\bullet}\cdot[1MC+H_{N3'}]^{+}$ in reaction (2) exceeds that of $9MOG^{\bullet+}\cdot 1MC$ in reaction (1), or the combination of two. To look into what factor(s) is in play, we turned to the Rice-Ramsperger-Kassel-Marcus (RRKM) modeling.[31] The fundamental assumption of the RRKM theory is that energy is randomized and distributed statistically among all of the energetically accessible states at

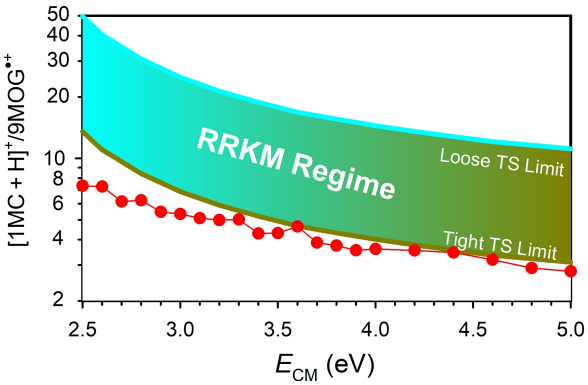

Figure 3. Comparison of product ion ratios in the Xe CID of $[9MOG\cdot 1MC]^{\bullet+}$ with RRKM predications. Red dots represent experimental data. The cyan solid line represents the loose-TS limit while the olive green line represents the tight-TS limit, and the area between represents the RRKM regime.

the transition state (TS) with no subsequent re-crossings,[32] and a statistical reaction occurs via minimum-energy pathway on the reaction potential energy surface, as the density of states is highest for such a pathway. The RRKM unimolecular rate constant (k_{diss}) is [Eq. (3)]:

$$k_{diss}(E,J) = \frac{d}{h}\frac{\sum_{K=-J}^{J} G[E - E_0 - E_r^{\dagger}(J,K)]}{\sum_{K=-J}^{J} N[E - E_r(J,K)]} \quad (3)$$

where E is the system energy, d is the reaction pathway degeneracy, h is the Planck's constant, G is the total number of accessible states at TS, N is the reactant density of states, J is the total angular momentum quantum number of the reaction system, K is the rotational quantum number, E_0 is the dissociation threshold, and E_r and $E_r^{\dagger}$ are rotational energies of

reactant and TS, respectively. J was treated as a good quantum number and conserved in the calculations, and $(2J+1)$ K-levels were all active and counted toward $k_{diss}(E,J)$.

In a statistical framework, the densities of states of $9MOG^{\bullet+}\cdot 1MC$ and $[9MOG - H_{N1}]^{\bullet}\cdot[1MC+H_{N3'}]^{+}$ at a specific E_{CM} correlate with their relative populations at that energy,[32] the ratio of $\frac{[1MC+H]^+}{9MOG^{\bullet+}}$ can therefore be evaluated as $\frac{N_{[9MOG-H_{N1}]^{\bullet}\cdot[1MC+H_{N3'}]^+}\times k_{[9MOG-H_{N1}]^{\bullet}\cdot[1MC+H_{N3'}]^+}}{N_{9MOG^{\bullet+}\cdot 1MC}\times k_{9MOG^{\bullet+}\cdot 1MC}}$ at each E_{CM}, where N is density of states and k is dissociation rate constant. The base-pair dissociation occurs at product asymptote and there is no reverse barrier. To this end, we assumed two types of TSs for the RRKM calculations, *i.e.*, *tight*- versus *loose*-TS.[33] In the *tight*-TS model, vibrational frequencies of the TS were taken from the parent base pair except that the symmetric stretching frequency of intra-base pair H-bonds was removed as it corresponds to the dissociation reaction coordinate (RC). In the *loose*-TS model, all the base-pair frequencies that are partitioned into dissociation products are conserved, which account for a total of (3 × atom number − 12) vibrational modes. The remaining 6 base-pair vibrational frequencies are associated with inter-base motions (out-of-plane butterfly bending, out-of-plane twisting, in-plane bending/gearing, *anti*-symmetric out-of-plane bending/step, symmetric stretching and *anti*-symmetric stretching). Among these, the symmetric stretching (the dissociation RC) was removed, and the remaining 5 modes were converted to transitional and rotational motions in the products. Their frequencies were scaled by a factor of 0.5 to account for the looseness of TS and the dissociation entropy. According to the literature work, this scaling factor was appropriate for modeling dissociation of weakly bonded complexes such as metal(ligand)$_n$ complexes.[33b–d] We also tried orbiting TSs[33a] for base-pair dissociation. The orbiting TSs are defined as loose TSs located at the centrifugal barrier which correspond to a loose association of products. The TSs assume that the dissociation frequencies are all converted to rotations in products. However, the dissociation ks estimated from the orbiting TSs were unrealistically slower than the ion time of flight (TOF) in mass spectrometer, suggesting the orbiting TSs are not appropriate to describe base-pair dissociation. This is because the base-pair H-bonding is much stronger than typical ion-molecule interaction.

Two sets of RRKM calculations were carried out using the *tight*- and *loose*-TSs, respectively. The results are compared in Figure 3. In both *tight*- and *loose*-TS models, $[9MOG - H_{N1}]^{\bullet}\cdot[1MC+H_{N3'}]^{+}$ dissociates faster than $9MOG^{\bullet+}\cdot 1MC$ by a factor of 3–4. On the other hand, $9MOG^{\bullet+}\cdot 1MC$ is dominating over $[9MOG - H_{N1}]^{\bullet}\cdot[1MC+H_{N3'}]^{+}$. The combination of ks and Ns allows us to propose a RRKM regime as highlighted in Figure 3. The top boundary of the regime is set by the *loose*-TS limit, while the bottom boundary is set by the *tight*-TS limit. The range for predicted product ratio at any E_{CM} spans a factor of 3 from one limit to the other. Any product ratio located within this regime can be described as statistical mechanism mediated. Qualitatively, the RRKM model reproduced the two trends in the experiment: the product ions $[1MC+H]^+$ are dominating, and the ratio of $\frac{[1MC+H]^+}{9MOG^{\bullet+}}$ decreases with increasing E_{CM}. Quantitively, the experimental product ratio seems approaching the lower, *tight*-TS limit at high energies. Yet, at $E_{CM} < 3$ eV, the experimental ratio is at least a factor of 2 lower than the RRKM prediction. The deviation between the experiment and RRKM becomes small toward high E_{CM}; but at the high E_{CM}, the reaction became more direct rather than complex-mediated, so the statistical assumption may not be fully valid. In this sense, the low-energy reaction behavior is a more sensible probe and it suggests that the reaction is at least *not fully* controlled by a statistical mechanism.

In our previous study, the WC type $[9MG\cdot 1MC - H]^-$,[34] $[9MG\cdot 1MC+H]^+$,[35] $[9MG\cdot 9MG]^{\bullet+}$,[36] $[9MOG\cdot 9MG]^{\bullet+}$,[36] and $[9MG\cdot 1MC]^{\bullet+}$[26] were all found to behave non-statistically in CID. In all of these cases, CID products from a PT base-pair conformer dominate over those produced from a conventional base-pair conformer, despite that the two conformers have similar dissociation thresholds. Interestingly, the CID of HG type $[9MG\cdot 1MC+H]^+$ follows a statistical mechanism.[37] Those results led us to hypothesize that non-statistical dissociation kinetics is the nature of WC base pairs. Non-statistical dissociation is accompanied with an characteristic intra-base pair PT originating from the N1–H at the WC-edge. The present work has provided a new supporting case.

2.2. Dissection of Singlet Oxygenation to $[9MOG\cdot 1MC]^{\bullet+}$

2.2.1. Oxidation Product Ions and Cross Sections

Guided by the base-pair CID results as well as our previous work on the $^1O_2$ oxidation of the monomeric $9MOG^{\bullet+}$,[18l] the present work measured the $^1O_2$ reaction with the $[9MOG\cdot 1MC]^{\bullet+}$ base pair. The measurement was carried out over an E_{CM} range of 0.02–0.2 eV. Results are summarized in Figure 4. The inset in the figure demonstrates a product ion mass spectrum acquired at $E_{CM}=0.02$ eV. Product ions were detected only at m/z 338, corresponding to a $[9MOG\cdot 1MC]^{\bullet+}$

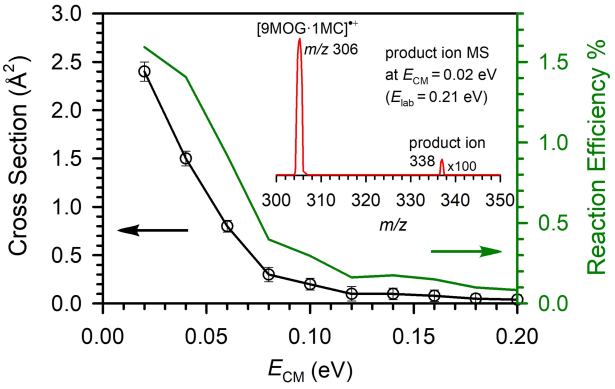

Figure 4. Product ion cross section (left axis) and reaction efficiency (right axis) of $[9MOG\cdot 1MC]^{\bullet+} + {}^1O_2$ as a function of E_{CM}. Inset shows a product ion mass spectrum measured at $E_{CM}=0.02$ eV.

$-O_2$ adduct. Product ion cross section was plotted as function of E_{CM}, and error bars were determined from five sets of measurements. The cross section is up to 2.4 Å^2 at the lowest E_{CM} but decreases at high energies, representing the energy dependence of an exothermic, barrierless ion-molecule reaction. The reaction efficiency for $[9MOG\cdot 1MC]^{\bullet+}$ toward $^1O_2$ was calculated as the ratio of product ion cross section to $\sigma_{collision}$. $\sigma_{collision}$ was taken the greater of the ion-induced dipole capture collision cross section[38] and hard-sphere collision cross section. The hard-sphere cross section was determined using the aforementioned projection area method available in *IMoS*. The resulting reaction efficiency was plotted in dark green in the figure (against the right axis). The efficiency reaches 1.6% at $E_{CM} = 0.02$ eV, 1.2% at 0.05 eV and decreases dramatically to 0.4% at 0.8 eV, becoming negligible above 0.10 eV.

One aim of the present measurement is to mimic and reveal the effects of local base-pair environment in *ds* DNA on the reactivity of $9MOG^{\bullet+}$ toward oxidation. It is thus informative to review the reaction outcome of $^1O_2$ with single $9MOG^{\bullet+}$.[18l] Similarly, the $^1O_2$ oxidation of $9MOG^{\bullet+}$ formed an O_2-adduct through an exothermic pathway and has no reaction activation barrier above the reactants. The reaction efficiency of $^1O_2$ with $9MOG^{\bullet+}$ reaches 2.3–2.5% at $E_{CM} = 0.05$–0.15 eV, gradually drops to 2% at 0.2 eV and 1% at 0.33 eV, and becomes $< 0.3\%$ at $E_{CM} \geq 0.5$ eV. Compared to $9MOG^{\bullet+}$, the reactivity of $[9MOG\cdot 1MC]^{\bullet+}$ toward $^1O_2$ drops significantly (by more than a factor of 2 at 0.05 eV), and the product ion cross section declines much faster at high E_{CM}. This resembles the type I oxidation reactivity of $OG^{\bullet+}$ nucleoside $\geq OG^{\bullet+}$ in *ss* oligonucleosides $>$ $[OG\cdot C]^{\bullet+}$ reported by Burrows and co-worker.[22] At first glance, the lower reactivity of the base pair might be explained by the steric hinderance of the complementary nucleobase. Nevertheless, the equilibrium of $9MOG^{\bullet+}\cdot 1MC \rightleftharpoons [9MOG - H_{N1}]^{\bullet}\cdot[1MC + H_{N3}]^{+}$ brings about two different forms of 9MOG radicals. It is necessary to first distinguish the individual $^1O_2$ oxidizability of $9MOG^{\bullet+}$ versus $[9MOG - H]^{\bullet}$.

2.2.2. Reaction Coordinates and Potential Energy Diagrams for $^1O_2$ with $9MOG^{\bullet+}$ versus $[9MOG - H]^{\bullet}$ and those in the Base Pair

Benchmark Approximately Spin-Projected (AP)-Density Functional Theory (DFT), CASPT2 and NEVPT2. One challenge in modeling the $^1O_2$ reactions is that, due to spin contamination arising from the low-energy lying $^3O_2$ state, single-reference DFT is not able to correctly describe the multireference character of $^1O_2$[39] as well as its addition to the doublet, open-shell $9MOG^{\bullet+}$. As a consequence, the DFT-calculated $9MG^{\bullet+}$–$^1O_2$ adduct not only suffered from spin contamination of a lower-energy lying quartet-state $^4[9MOG^{\bullet+}(\uparrow)\cdots{}^3O_2(\uparrow\uparrow)]$ (see Scheme S3 in the Supporting Information for doublet and quartet electron configurations), but also converged to a lower-energy but incorrect doublet-state $^2[9MOG^{\bullet+}(\downarrow)\cdots{}^3O_2(\uparrow\uparrow)]$. These two states are distinctively different than the correct but higher-energy lying doublet-state $^2[9MOG^{\bullet+}(\uparrow)\cdots{}^1O_2(\uparrow\downarrow)]$. The spin contamination was quantitively evaluated using the CCSD(T) T1 diagnostic.[40] A T1 value that is larger than 0.02 for a closed-shell system or larger than 0.03 for an open-shell system indicates severe multiconfigurational characters or nondynamical correlation effects, which require other important configurations as references in the treatment of nondynamic electron correlation.[40a] In the case of $9MOG^{\bullet+} + {}^1O_2$, not only the $^1O_2$ reactant (T1 = 0.015) and the early-stage reaction precursor complex (0.026) suffer from spin contamination but also the TSs (T1 = 0.02–0.026) for various O_2-addition routes. To acquire accurate electronic structures and reaction potential energies, we have tried two different approaches. The first approach was to apply the Yamaguchi's approximate spin projection (AP)[41] to the ωB97XD functional in reaction structure optimization and the second approach was to employ multireferential electronic structure theories. Two multireferential theories were chosen, including the CASPT2[42] method which adds dynamical correlations to the conventional complete active space self-consistent-field method (CASSCF)[43] using 2nd-order perturbation theory, and the *N*-electron valence state 2nd-order perturbation theory (NEVPT2).[44] Note that the conventional CASSCF method was not chosen, as CASSCF includes primarily static electron correlation and consequently overestimated reaction energies and activation barrier in the $^1O_2$ reactions with neutral guanine[45] and guanine radical cation.[46]

We have previously proposed probable reaction pathways for the $^1O_2$ oxidation of $9MOG^{\bullet+}$.[18l] These include C4- and C5-terminal addition of O_2 to $9MOG^{\bullet+}$ and subsequent formation of 4- and 5-hydroperoxides, concerted 2,4-cycloaddition across the dienophile C2–C4 bond of $9MOG^{\bullet+}$, and H-abstraction of $9MOG^{\bullet+}$ by $^1O_2$ to dehydrogenated $[9MOG - H]^{+}$ and $HOO^{\bullet}$ followed by product recombination to form 4-hydroperoxides. These pathways are presented in Scheme S4 in the Supporting Information. Reaction energies for these pathways were calculated at AP-ωB97XD/6-31 + G(d,p), CASPT2(21e,15o)/6-31G(d,p) and NEVPT2(15e,12o)/6-31 + G(d,p), respectively. Energy results are compiled in Table S2 in the Supporting Information, and variances between difference theories are compared in Table S3 in the Supporting Information. The AP-ωB97XD-calculated reaction energies closely match the CASPT2 energies, and their differences are between −0.30 and + 0.40 eV. For most reaction species, the CASPT2 energy is about 0.02–0.3 eV lower than the AP-ωB97XD value. The exceptions are **TS**5OOH$_{N7}$, **TS**4OOH$_{N1}$, **TS**4OOH$_{N2}$, **TS**4OOH$_{N7}$ and **TS**24, for which the CASPT2 energies are 0.1 eV or more higher than AP-ωB97XD. Both AP-ωB97XD and CASPT2 have predicted that *anti-*/*syn*-5-OO-$9MOG^{\bullet+}$ (indicated bold in Table S2, and *anti-*/*syn-* refer to the orientation of the peroxide group with respect to the imidazole ring) are the only exothermic products with activation barriers below the reactants. The other pathways require higher activation energies and/or larger product formation endothermicities. NEVPT2, on the contrary, has predicted that all product pathways are endothermic (or have a high-energy barrier). Considering that an exothermic O_2-addition was indeed observed in our experiment,[18l] we concluded that NEVPT2 has badly overestimated reaction energies. The large energy

difference between the CASPT2 and NEVPT2 calculations in this work may be caused by the smaller active space being used for the NEVPT2 calculations as a trade-off between accuracy and cost. In the following work, only AP-ωB97XD and CASPT2 were used.

Comparison of $^1O_2$ with 9MOG$^{\bullet+}$ versus [9MOG − H]$^\bullet$. The ion-beam experiment could not measure the reactivity of neutral [9MOG − H]$^\bullet$ directly. To this end, computation has provided a useful guidance on [9MOG − H]$^\bullet$ versus 9MOG$^{\bullet+}$ in the singlet oxygenation reaction. The right portion of Table S2 in the Supporting Information presents the reaction results for [9MOG − H]$^\bullet$ + $^1O_2$. Pathways and products of the same type in 9MOG$^{\bullet+}$ + $^1O_2$ versus [9MOG − H]$^\bullet$ + $^1O_2$ are listed side by side in Table S2. Scheme S5 in the Supporting Information portrays the reaction pathways for the $^1O_2$ addition to [9MOG − H]$^\bullet$. [9MOG − H]$^\bullet$ reproduces nearly all of the pathways of 9MOG$^{\bullet+}$ except that [9MOG − H]$^\bullet$ does not have C4-O_2 addition, formation of 5-OOH$_{N1}$ hydroperoxide, or H_{N2}-abstraction. However, those pathways are the least favorable for 9MOG$^{\bullet+}$; therefore, they are not likely to result in a noticeable difference in the reactivities of 9MOG$^{\bullet+}$ versus [9MOG − H]$^\bullet$. The dominating similarity between 9MOG$^{\bullet+}$ and [9MOG − H]$^\bullet$ is that both favor C5-O_2 addition, despite that the energies of *syn-/anti*-[5-OO-9MOG − H]$^\bullet$ are about 0.2–0.35 eV lower than those of *anti-/syn*-[5-OO-9MOG]$^{\bullet+}$. Their differences are: (1) the remaining pathways of [9MOG−H]$^\bullet$ are more than 0.35 eV lower in energy than those of 9MOG$^{\bullet+}$; (2) formation of [9MOG − H_{N7}]$^+$ + HOO$^\bullet$ is endothermic in 9MOG$^{\bullet+}$ but the same reaction becomes exothermic in [9MOG − H]$^\bullet$; and (3) [9MOG − H]$^\bullet$ presents new, 2,5-cycloaddition. These findings serve as reference points for understanding radical reactivities within a base-pair context.

Reaction Pathways and Potential Energy Diagram for the Base Pair. Finally, we analyze the $^1O_2$ reactions with 9MOG$^{\bullet+}$ ·1MC ⇌ [9MOG − H_{N1}]$^\bullet$·[1MC + $H_{N3'}$]$^+$. A ChemDraw schematic description of all probable reaction pathways for 9MOG$^{\bullet+}$·1MC and [9MOG − H_{N1}]$^\bullet$·[1MC + $H_{N3'}$]$^+$ is available in Schemes S6 and S7 in the Supporting Information. Their numerical results are summarized in Table 1.

The schematic reaction coordinates and potential energy diagram for these pathways are depicted in Figure 5. The GaussView structures in the bottom of Figure 5 compare reaction structures for 9MOG$^{\bullet+}$·1MC with their analogues for [9MOG − H_{N1}]$^\bullet$·[1MC + $H_{N3'}$]$^+$. We adopt the similar nomenclatures for the intermediate and TS in the same type of reaction but use suffix (PT) to distinguish. The potential energy diagram displays the two sets of reaction energies which were calculated using AP-ωB97XD/6-31 + G(d,p) and CASPT2/631G(d,p), respectively. At both levels of theory, the product *syn-/anti*-5OO has activation barrier located below reactants (*i.e.*, barrierless), the [9MOG − H_{N7}]$^+$ + HOO$^\bullet$ and [9MOG − H_{N1} − H_{N7}] + HOO$^\bullet$ are near thermal, whereas the formation of 5OOH$_{N1}$ and 5OOH$_{N7}$ requires high activation barrier.

2.3. Interplay between Intra-Base Pair PT and Singlet Oxygenation

Comparison of the $^1O_2$ oxidation of the monomeric radicals versus those within the base pair provides the knowledge of how structural context influences DNA oxidative damage. Influences of base-pairing on singlet oxygenation and the interplay with intra-base pair PT are reflected in many aspects:

(1) Effect of intra-base pair PT (9MOG$^{\bullet+}$·1MC versus [9MOG − H_{N1}]$^\bullet$·[1MC + $H_{N3'}$]$^+$): Reaction pathways of $^1O_2$ with the two base-pair conformers are mostly identical, except for the lack of 5-OOH$_{N1}$ formation in [9MOG − H_{N1}]$^\bullet$·[1MC + $H_{N3'}$]$^+$. For both base pairs, the formation of 5-peroxides represents

Table 1. Reaction energies (eV, all are with respect to 9MOG$^{\bullet+}$·1MC + $^1O_2$) for $^1O_2$ with 9MOG$^{\bullet+}$·1MC and [9MOG − H_{N1}]$^\bullet$·[1MC + $H_{N3'}$]$^+$, calculated at different levels of theory. Products indicated in bold represent the most probable ones detected in the experiment.

radical cations	AP-ωB97XD	CASPT2	neutral radicals	AP-ωB97XD	CASPT2
9MOG$^{\bullet+}$·1MC + $^1O_2$	0.00	0.00	[9MOG − H_{N1}]$^\bullet$·[1MC + $H_{N3'}$]$^+$ + $^1O_2$	0.03	0.03
precursor	−0.35	–	precursor	−0.34	–
			C5-addition		
syn-/anti-**TS**5	−0.80 / −0.74	−1.05 / −0.91	*syn-/anti*-**TS**5	−0.82 / −0.76	−1.03/ −1.03
***syn-/anti*-[5-OO-9MG]$^{\bullet+}$**	**−0.86 / −0.86**	**−0.93 / −0.99**	***syn-/anti*-[5-OO-9MG − H_{N1}]$^\bullet$**	**−0.90 / −0.89**	**−0.99 / −1.05**
TS5OOH$_{N1}$	1.39	1.66			
[5-OOH$_{N1}$-9MOG]$^{\bullet+}$	0.70	0.75			
			H-abstraction		
TSOOH$_{N2}$	1.45	1.33	**TS**OOH$_{N2}$(PT)	1.30	1.08
[9MOG − H_{N2}]$^+$ + HOO$^\bullet$	1.52	1.35	[9MOG − H_{N1} − H_{N2}] + HOO$^\bullet$	1.38	1.16
TS5OOH$_{N2}$	1.67	1.61	**TS**5OOH$_{N2}$(PT)	1.68	1.43
[5-OOH$_{N2}$-9MOG]$^{\bullet+}$	0.74	0.59	[5-OOH$_{N2}$-9MOG − H_{N1}]$^\bullet$	0.74	0.67
TSOOH$_{N7}$	0.09	−0.22	**TS**OOH$_{N7}$(PT)	0.09	−0.24
[9MOG − H_{N7}]$^+$ + HOO$^\bullet$	0.05	−0.27	[9MOG − H_{N1} − H_{N7}] + HOO$^\bullet$	0.09	−0.23
TS5OOH$_{N7}$	0.72	0.53	**TS**5OOH$_{N7}$(PT)	0.72	0.55
[5-OOH$_{N7}$-9MOG]$^{\bullet+}$	0.36	0.25	[5-OOH$_{N7}$-9MOG − H_{N1}]$^\bullet$	0.33	0.17
			2,4-cycloaddition		
TS24	1.92	1.92	**TS**24(PT)	1.79	1.75
[2,4-OO-9MOG]$^{\bullet+}$	1.82	1.70	[2,4-OO-9MOG − H_{N1}]$^\bullet$	1.68	1.56

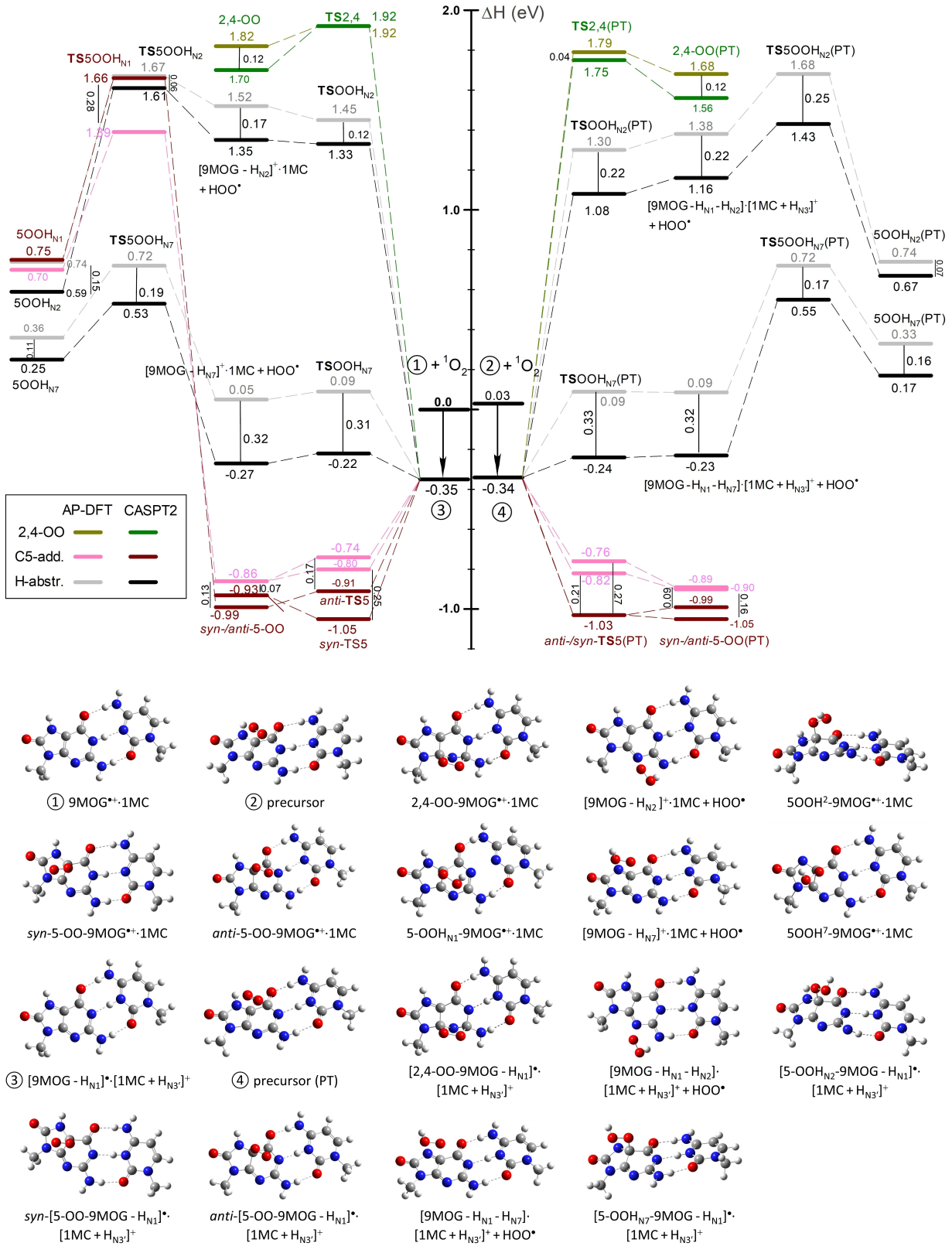

Figure 5. Singlet O_2 reaction coordinates, potential energy diagram, and structures for $9MOG^{\bullet+}\cdot 1MC$ and $[9MOG - H_{N1}]^{\bullet}\cdot[1MC + H_{N3'}]^{+}$. Reaction enthalpies were calculated at AP-ωB97XD/6-31 + G(d,p) and CASPT2/6-31G(d,p)//ωB97XD/6-31 + G(d,p), respectively, including 298 K thermal corrections. Energy differences between the two levels of theory are indicated by black vertical lines in the diagrams. Different reaction pathways are distinguished using different colors.

the energetically most probable, followed by H_{N7}-abstraction. The experiment ruled out endothermic channels including 2,4-cycloaddition, H_{N2}-abstraction, and 5-OOH_{N1} and 5-OOH_{N7} hydroperoxides.

(2) Effect of base pairing ($9MOG^{\bullet+}\cdot 1MC$ versus $9MOG^{\bullet+}$, and $[9MOG - H_{N1}]^{\bullet}\cdot[1MC + H_{N3'}]^{+}$ versus $[9MOG - H]^{\bullet}$): The reaction diversity of $9MOG^{\bullet+}\cdot 1MC$ toward $^1O_2$ appears to be similar to that of the monomeric $9MOG^{\bullet+}$. The major difference is that in $9MOG^{\bullet+}$, the 5-OOH_{N2} and 5-OOH_{N7} are formed following the formation of 5-OO peroxides, whereas in $9MOG^{\bullet+}\cdot 1MC$, the formation of the same 5-OOH hyperoxides are mediated by the recombination of the H-abstraction product and $HOO^{\bullet}$. Similarly, in the case of $[9MOG - H_{N1}]^{\bullet}\cdot[1MC + H_{N3'}]^{+}$ versus $[9MOG - H]^{\bullet}$ with $^1O_2$, the formation of 5-OOH_{N2} and 5-OOH_{N7} hydroperoxides are mediated by 5-OO peroxides in the monomer whereas preceded by H-abstraction in the base pair. Furthermore, 2,5-cycloaddition is present in the monomer but missing in the base pair.

(3) Electrostatic effect ($9MOG^{\bullet+}$ versus $[9MOG - H]^{\bullet}$, and $9MOG^{\bullet+}\cdot 1MC$ versus $[9MOG - H_{N1}]^{\bullet}\cdot[1MC + H_{N3'}]^{+}$): In the monomeric forms, $[9MOG - H]^{\bullet}$ presents up to 1.1 eV favorability in reaction energetics than $9MOG^{\bullet+}$. In the base-pair context, $[9MOG - H]^{\bullet}\cdot[1MC + H]^{+}$ is only up to 0.25 eV more favorable in reaction energetics than $9MOG^{\bullet+}\cdot 1MC$. This implies a preference for the O_2 attack upon a neutral $[9MOG - H]^{\bullet}$ moiety, but the preference becomes less in duplex DNA.

(4) Effect on reaction pathways ($9MOG^{\bullet+}$ versus $[9MOG - H]^{\bullet}$ and those in the base pair): The 4-peroxide, and the 4-OOH_{N1} and 4-OOH_{N2} hydroperoxides only form in the singlet oxygenation of the monomeric $9MOG^{\bullet+}$ but not in the monomeric $[9MOG - H]^{\bullet}$ or any base pairs. The 4-OOH_{N7} hydroperoxide is formed in both the $9MOG^{\bullet+}$ and $[9MOG - H]^{\bullet}$ monomers but again not in any base pair. This supports the fact that the base-pair structure leads to lower accessibility for O_2 addition.

(5) Effect on base-pairing energy: Singlet oxygenation slightly increases base-pairing energy in a conventional structure whereas significantly decreases base-pairing energy in a PT structure. The pairing energy (with BSSE correction) is 2.16 eV for $9MOG^{\bullet+}\cdot 1MC$ versus 2.03 eV for $[9MOG - H_{N1}]^{\bullet}\cdot[1MC + H_{N3'}]^{+}$. After the O_2 addition, it becomes 2.31 eV for 5-OO-$9MOG^{\bullet+}\cdot 1MC$ versus 1.84 eV for $[5\text{-}OO\text{-}9MOG - H_{N1}]^{\bullet}\cdot[1MC + H_{N3'}]^{+}$.

(6) Effect on overall reactivity: The reaction energies (activation barriers and product enthalpies) of $[9MOG - H_{N1}]^{\bullet}\cdot[1MC + H_{N3'}]^{+}$ with $^1O_2$ are more favorable than those of $9MOG^{\bullet+}\cdot 1MC$. The implication is that the PT conformation becomes more stable than the conventional one in an oxidized base pair.

The comparison of isolated versus base-pair radicals in different charge states is more informative. In the case for the main product 5-peroxide, $[5\text{-}OO\text{-}9MOG]^{\bullet+}\cdot 1MC$ is 0.1–0.15 eV lower than the monomeric 5-OO-$9MOG^{\bullet+}$, whereas $[5\text{-}OO\text{-}9MOG - H_{N1}]^{\bullet}\cdot[1MC + H_{N3'}]^{+}$ is 0.1–0.2 eV higher than $[5\text{-}OO\text{-}9MOG - H]^{\bullet}$. What is more remarkable is the H_{N7}-abstraction. The reaction of $9MOG^{\bullet+}\cdot 1MC + {}^1O_2 \rightarrow [9MOG - H_{N7}]^{+}\cdot 1MC + HOO^{\bullet}$ is exothermic (or near thermal). For comparison, the reaction of $9MOG^{\bullet+} + {}^1O_2 \rightarrow [9MOG - H_{N7}]^{+} + HOO^{\bullet}$ increases the energy by more than 0.2 eV and becomes endothermic. The same reaction remains marginally exothermic or endothermic (depending on the calculation levels of theory) for $[9MOG - H]^{\bullet}$ and $[9MOG - H_{N1}]^{\bullet}\cdot[1MC + H_{N3'}]^{+}$. The experimental and theoretical findings lead to the order of reactivity: $[9MOG - H]^{\bullet} > 9MOG^{\bullet+} > [9MOG - H_{N1}]^{\bullet}\cdot[1MC + H_{N3'}]^{+} > 9MOG^{\bullet+}\cdot 1MC$.

3. Conclusions

The 8-oxoguanosine−cytidine base pair represents a common DNA lesion. Failure to remove OG and restore the correct G·C code before replication not only leads to formation of HG OG·A(adenosine) base pair[47] and ultimately G → T(thymidine) transversion mutations,[48] but also renders the base pair more vulnerable to ionizing radiation, singlet oxygenation and other oxidative damage. This work examined the reaction kinetics and thermodynamics for the intra-base pair proton transfer, dissociation and singlet oxygenation of the Watson−Crick base-pair radical cation $[9MOG\cdot 1MC]^{\bullet+}$. The non-statistical dissociation of $[9MOG\cdot 1MC]^{\bullet+}$ in collisions with Xe was discovered in terms of $[9MOG - H_{N1}]^{\bullet}\cdot[1MC + H_{N3'}]^{+} \rightarrow [9MOG - H_{N1}]^{\bullet} + [1MC + H_{N3'}]^{+} \gg 9MOG^{\bullet+}\cdot 1MC \rightarrow 9MOG^{\bullet+} + 1MC$, and the ratio of $\frac{[1MC+H]^{+}}{9MOG^{\bullet+}}$ significantly deviates from a statistic RRKM prediction. This result suffices a new supporting case to our previous findings that non-statistical CID is characteristic of Watson−Crick base-pair ions containing guanine and/or 8-oxoguianine, and provides insight into base-pairing structure. The reaction of $[9MOG\cdot 1MC]^{\bullet+}$ with $^1O_2$ produced an exothermic O_2-adduct. The reaction efficiency reaches only 1.6% at the center-of-mass collision energy of 0.02 eV and declines quickly with increasing collision energy, becoming negligible above 0.10 eV. This efficiency is more than a factor of 2 lower than that of the monomeric $9MOG^{\bullet+}$. To distinguish and disentangle the contributions of $9MOG^{\bullet+}\cdot 1MC$ versus $[9MOG - H_{N1}]^{\bullet}\cdot[1MC + H_{N3'}]^{+}$ to the reaction with $^1O_2$ and the base-pair structural effects on the reaction, reaction pathways and energies of individual base-pair conformers and the monomeric $9MOG^{\bullet+}$ and $[9MOG - H]^{\bullet}$ were mapped out using approximately spin-projected DFT and CASPT2. The combined experimental and theoretical results have pinpointed a few key factors: 1) both single nucleobases and base pairs lead to 5-OO peroxides as the most probable products in the initial $^1O_2$ oxidation, and this pathway has no barrier above reactants; 2) H_{N7}-abstraction becomes thermodynamically feasible for $[9MOG - H]^{\bullet}$ which leads to $[9MOG - H_{N1} - H_{N7}] + HOO^{\bullet}$, but the same pathway does not open to $9MOG^{\bullet+}$. Interestingly, H_{N7}-abstraction becomes feasible in both $9MOG^{\bullet+}\cdot 1MC$ and $[9MOG - H_{N1}]^{\bullet}\cdot[1MC + H_{N3'}]^{+}$; 4) the reactions of $[9MOG - H]^{\bullet}$ is more energetically favorable than those of $9MOG^{\bullet+}$ both in monomers and in a base-pair context. The combined results

lead to the order of reactivity as $[9MOG - H]^{\bullet} > 9MOG^{\bullet+} > [9MOG - H_{N1}]^{\bullet} \cdot [1MC + H_{N3'}]^{+} \geq 9MOG^{\bullet+} \cdot 1MC$.

Experimental and Computational Section

All chemicals were used as supplied: 9MOG (received as a gift from Dr. Bernhard Lippert at University of Dortmund, Germany),[49] 1MC (Enamine, 95%), $Cu(NO_3)_2$ (Alfa Aesar, 99.999%), KOH (Fisher Chemical, >85%), and 35 wt.% H_2O_2 (Acros Organics). The Xe gas (99.995%) was purchased from Spectral Gases, the He gas (research grade) was purchased from T.W. Smith, and the Cl_2 gas (≥99.5%) was from Sigma-Aldrich. All the solvents used were HPLC grade.

Formation and reactions of $[9MOG \cdot 1MC]^{\bullet+}$

Tandem CID Mass Spectrometric Experiment. The experiment was carried out on a home-built tandem mass spectrometer coupled with an electrospray ionization (ESI) source.[27] Details of instrumentation including calibration, data collection and analysis were described previously. The base-pair radical cations $[9MOG \cdot 1MC]^{\bullet+}$ were prepared by collision-induced redox-separation of Cu^{II}-base-pair complexes in the gas phase. This nucleobase radical cation generation method was first reported by O'Hair,[50] Bohme[51] and their co-workers. The same method was adopted in the formation of base-pair radical cations of WC guanosine−cytidine and guanosine/deoxyguanosine homodimers and heterodimers by O'Hair group[52] and in the formation of $[9MG \cdot 1MC]^{\bullet+}$,[26] $[9MG \cdot 9MG]^{\bullet+}$,[36] $[9MOG \cdot 9MG]^{\bullet+}$,[36] and $[9MOG \cdot 9MOG]^{\bullet+}$[36] in our laboratory. The Cu^{II}-base-pair complexes were formed in a methanol/water (v/v 3:1) solution containing 0.25 mM 9MOG, 0.25 mM 1MC and 0.25 mM $Cu(NO_3)_2$. The solution was sprayed into ambient atmosphere through an ESI needle (biased at ~2.35 kV with respect to the ground) at a flow rate of 0.06 mL/h. The positively charged droplets containing doubly charged copper nucleobase complexes $[Cu^{II}(9MOG)_m(1MC)_n]^{2+}$ entered a heated (190 °C) desolvation capillary through an 0.23 mm-diameter entrance aperture of the mass spectrometer, and were converted into gaseous complexes throughout the capillary. The desolvation capillary was biased at 130 V relative to the ground. A skimmer of 1.0 mm-diameter orifice was located at 3 mm away from the end of the capillary and biased at 23 V relative to the ground. The electrical potential difference between the capillary and the skimmer promoted collision-induced dissociation of the gaseous Cu^{II}-base pair complexes with the background gas (at a pressure of 1.7 Torr) in the source chamber of the mass spectrometer, of which the redox-separation of $[Cu^{II}(9MOG \cdot 1MC)_3]^{\bullet 2+}$ led to the formation of $[Cu^{I}(9MOG \cdot 1MC)_2]^{+}$ and $[9MOG \cdot 1MC]^{\bullet+}$.

Ions including $[9MOG \cdot 1MC]^{\bullet+}$ were guided through the skimmer to a radio frequency (rf) hexapole ion guide and had thermalizing collisions with the background gas within the hexapole (at a pressure of 20 mTorr). Internal energies of the thermalized ions could be described by a Maxwell−Boltzmann distribution at 310 K. The ions were then focused into and mass-selected by the first quadrupole mass filter in the tandem mass spectrometer. The mass-selected $[9MOG \cdot 1MC]^{\bullet+}$ ions were collimated by a set of electrostatic lenses into a rf octopole ion guide where ions were radially trapped by rf potential. In addition to the rf potential, a DC bias voltage was applied on the octopole to accelerate/deaccelerate the ion beam at the octopole entrance to a desired kinetic energy in the laboratory frame (E_{lab}). The latter was used to control the center-of-mass collision energy (E_{CM}) between $[9MOG \cdot 1MC]^{\bullet+}$ and Xe gas, *i.e.*, $E_{CM} = E_{lab} \times \frac{m_{neutral}}{(m_{ion}+m_{neutral})}$ wherein $m_{neutral}$ and m_{ion} are the masses of the neutral reactant gas and reactant ion, respectively. The $[9MOG \cdot 1MC]^{\bullet+}$ ions then passed through the octopole that is surrounded by a scattering cell containing the Xe target gas for collision-induced dissociation. The pressure of the Xe gas within the scattering cell was maintained at 0.015 mTorr. With this pressure, the base-pair ions had at most single collisions with Xe. The probability for single ion-neutral collisions was 3%, and that for multiple ion-neutral collisions was negligible (<0.09%). After ion-neutral collisions, the product ions and the remaining base-pair reactant ions were collected by the octopole and directed to the second quadrupole mass filter in the tandem mass spectrometer for mass analysis and pulse-counted by an electron multiplier.

The intensity of the $[9MOG \cdot 1MC]^{\bullet+}$ ion beam was 1.4×10^4 counts per sec. The kinetic energy spread (full width at half maximum, FWHM) of the ion beam was determined to be 0.65 eV based on a retarding potential analysis.[27,53] Under our thin-target collision conditions, reaction cross section (σ, a micro-analogue of rate constant, and σ is equal to rate constant/relative velocity between reactants[28b]) was determined by Beer–Lambert law,[28c,54] *i.e.*, $\sigma = \frac{I_{product}\, k_B T}{I_{reactant}\, P_{cell}\, l_{cell}}$ where k_B is the Boltzmann constant, T is the temperature of reactants, $I_{product}/I_{reactant}$ is the ratio of product/reactant ion intensities, P_{cell} is the target gas pressure in the scattering cell, and l_{cell} is the effective cell length. The CID measurement was cycled through a wide range of E_{CM} from 0.05 to 5.0 eV. The experiment was repeated for at least five times, and the relative uncertainty (when comparing cross sections at difference E_{CM}) was less than 5%.

Analysis of CID Threshold Energy at 0 K. Due to the kinetic energy spread and the internal energy of the reactant ion beam and the Doppler broadening (*i.e.*, thermal velocity inside the scattering cell) of the Xe gas, the cross section of CID product ions rises from zero at E_{CM} lower than the true dissociation threshold (E_0). To extract the true value of E_0, a modified line-of-center (LOC) model[28] was used[Eq. (4)]:

$$\sigma(E) = \sigma_0 \frac{(E_{CM} + E_{vib} + E_{rot} - E_0)^n}{E_{CM}} \quad (4)$$

where σ_0 is an energy-independent scaling factor, E_{CM} is as defined above, E_{vib} and E_{rot} are the reactant vibrational and rotational energies, E_0 is the dissociation threshold energy at 0 K, and n is a fitting parameter that describes the efficiency of translational-to-internal energy transfer ($T \rightarrow E_{int}$) in collisions. The LOC model assumes that at least some of near-threshold collisions are completely inelastic so that all energy is available to drive base-pair dissociation. This was verified in near-threshold CID studies of other base-pair systems[26,34–37] as well as in dissociation of other covalent molecules[55] and ionic complexes.[33c,d,56]

Before comparison with the experimental data, the $\sigma(E)$ function was convoluted over the experimental energy broadening of reactant ions and the Xe gas as well as kinetic factors. A Monte Carlo classical mechanics simulation program written for ion-molecule collisions[26,57] was used to mimic energy broadening in ion-Xe collision. For each product channel, a total of 100000 ion-Xe collisions were simulated at each nominal E_{CM}. In these collisions, the Xe atoms were sampling a Maxwell−Boltzmann kinetic energy distribution at the scattering cell temperature of 300 K. The primary ions were sampling E_{lab} (corresponding to specific E_{CM}) with a 0.7 eV FWHM in the laboratory frame and E_{vib} and E_{rot} from the normalized vibrational and rotational Maxwell−-Boltzmann energy distributions at 310 K.

To account for kinetic shift[33a] in CID (*i.e.*, excess energy is required to observe detectable dissociation within the ion TOF in the mass

spectrometer), each collision that had total energy exceeding E_0 was subjected to the RRKM analysis to determine if it would lead to a dissociation within the TOF (100 to 500 μs) or not. The collision outcomes at various E_{CM} were fed into Equation (4).

A leveling-off function was used in the fitting which allows $\sigma(E)$ to reach a plateau at high E_{CM}. The rising curvature of cross section is controlled by E_0 and n and their values were adjusted until the convoluted $\sigma(E)$ reproduced the experimental data. Uncertainties in the E_0 fitting were determined from several independent fits using an acceptable range of n (1.5–2.5) and included the absolute uncertainties (less than 0.10 eV) in E_{CM}.

Reaction of [9MOG·1MC]$^{\bullet+}$ with $^1O_2$. Singlet O_2 was generated in a chemical reaction $H_2O_2 + Cl_2 + 2KOH \rightarrow O_2[a^1\Delta_g]/O_2[X^3\Sigma_g^-] + 2KCl + 2H_2O$.[58] 10.5 mL of 8 M KOH was added dropwise to 20 mL of 35 wt.% H_2O_2 and the mixture was maintained at −20 °C using a recirculating chiller. The chilling removed the heat release in the mixing of KOH and H_2O_2 and prevented H_2O_2 decomposition. The Cl_2 and He gases (each at a constant flow rate of 3 and 53 mL/min, respectively) were mixed through a gas proportioner and introduced to the slushy H_2O_2/KOH. All Cl_2 reacted completely with H_2O_2 and produced the gas mixture of $^1O_2$ (15%), $^3O_2$ (85%) as well as the He carrier gas. The gas products passed through a second trap maintained at −70 °C to remove the containing water vapor. The pressure of the $^1O_2$ chemical reactor was maintained at 12.8 Torr to avoid significant O_2 self-quenching. Before leaking into the scattering cell, the absolute concentration of $^1O_2$ was determined by measuring its emission of $^1O_2$ ($a^1\Delta_g \rightarrow X^3\Sigma_g^-$, $v = 0$–0) at 1270 nm[59] using a home-built near-IR emission cell[58c] equipped with focusing lenses, a 1270-nm interference filter, a thermoelectrically cooled InGaAs photodetector, an optical chopper, and a lock-in-amplifier. The output from the lock-in amplifier was converted into absolute $^1O_2$ concentration on the basis of a previous calibration.

The $^1O_2/^3O_2$ and He were then leaked to the scattering cell using a leak valve. The cell gas pressure was maintained at 0.25 mTorr for the $^1O_2$ reaction, of which only 5% was $^1O_2/^3O_2$. The interaction of the remaining He gas with ions could be neglected in the reaction due to the light neutral-heavy ion combination. The literature[60] reported that nucleobase radical is not reactive with $^3O_2$. This was confirmed in our control experiment by using pure $^3O_2$ as the reactant gas.

Reaction Potential Energy Calculations

DFT, Couple cluster and RRKM for CID modeling. Electronic structures of 9MOG$^{\bullet+}$·1MC, [9MOG − H]$^{\bullet}$·[1MC + H]$^+$ and dissociation products were optimized using the ωB97XD functional paired with the 6-311++G(d,p) basis set. The range-separated ωB97XD functional provided reduced self-interaction errors and improved the orbital description of nucleobase radicals.[25] Reactants and products were confirmed to be stationary structures with no imaginary frequency. Transition state (TS) was verified by having only one imaginary frequency which corresponds to reaction coordinate. Basis set superposition errors (BSSEs) were estimated by the counterpoise correction[61] calculations. BSSEs were less than 0.05 eV and corrected for in the potential energy diagram. All DFT calculations were completed using Gaussian 16.[62]

Single-point energy calculations of the ωB97XD-optimized structures were complemented using the domain based local pair-natural orbital coupled-cluster theory including single and double excitation with a perturbative triple-excitation DLPNO-CCSD(T) method[63] coupled with the aug-cc-pVQZ basis set. The CCSD(T) theory is consider a "gold standard"[63–64] of quantum chemistry with accuracy comparable to experiments. The DLPNO-CCSD(T) calculations were accomplished using ORCA 4.2.1.[65] The reaction potential energy at 298 K includes electronic energy calculated at DLPNO-CCSD(T), zero-point energy (ZPE, scaled by a factor of 0.975[66]) and thermal corrections calculated at ωB97XD. For reaction energies at 0 K, only ZPEs were included in addition to electronic energies.

RRKM dissociation rates were calculated using the Zhu and Hase code of the RRKM program.[67] The Beyer-Swinehart direct-count algorithm[68] was used to calculate density of states. Vibrational frequencies, rotational constants, and moments of inertia of reactants and TSs needed in the RRKM calculations were all taken from the DFT calculations.

Approximately Spin-Projected DFT for Singlet Oxygenation Reactions. Reaction structures for 9MOG$^{\bullet+}$, [9MOG − H]$^{\bullet}$, 9MOG$^{\bullet+}$·1MC and [9MOG − H_{N1}]$^{\bullet}$·[1MC + $H_{N3'}$]$^+$ with $^1O_2$, including reactants, intermediate complexes, TSs and products were all computed at the ωB97XD/6-31+G(d,p) level of theory. Intrinsic reaction coordinate (IRC) calculations were carried out to ascertain that TSs are connected to correct reactant/product minima. Yamaguchi's approximate spin projection of the DFT energy was calculated by [Eq. (5)]:

$$E = \frac{\langle \hat{S}^2 \rangle^{HS} - \langle \hat{S}^2 \rangle^{BS}_{exact}}{\langle \hat{S}^2 \rangle^{HS} - \langle \hat{S}^2 \rangle^{BS}} E^{BS} - \frac{\langle \hat{S}^2 \rangle^{BS} - \langle \hat{S}^2 \rangle^{BS}_{exact}}{\langle \hat{S}^2 \rangle^{HS} - \langle \hat{S}^2 \rangle^{BS}} E^{HS} \quad (5)$$

where E^{BS} and $\langle \hat{S}^2 \rangle^{BS}$ refer to the DFT electronic energy and the average value of the total spin angular momentum operator for a broken symmetry, low-spin target state (before annihilation of spin contamination), and E^{HS} and $\langle \hat{S}^2 \rangle^{HS}$ represent the counterparts for a high-spin state. When spin contamination is negligible, $\langle \hat{S}^2 \rangle^{BS}$ is close to the exact value $\langle \hat{S}^2 \rangle^{BS}_{exact}$. The latter is defined as [Eq. (6)]:

$$\langle \hat{S}^2 \rangle^{BS}_{exact} = \frac{N^\alpha - N^\beta}{2}\left(\frac{N^\alpha - N^\beta}{2} + 1\right) \quad (6)$$

where N^α and N^β are the numbers of α and β electrons, respectively.

CASPT2 and NEVPT2 for Singlet Oxygenation Reactions. The CASPT2[42] and NEVPT2[44] single-point energies for the ωB97XD/6-31+G(d,p) optimized structures were calculated using OpenMolcas version 22.1.[69] In the CASPT2 calculations, 6-31G(d,p) was used as the basis set. The active space for $^1O_2$-adducts and TSs was set to 21 electrons and 15 orbitals (21e,15o), which includes (12e,8o) from the $^1O_2$ moiety and (9e,7o) from the nucleobase or base-pair radicals. A potential drawback of CASPT2 concerns an intruder state in which the zero-order energy associated to the CASSCF wavefunction is nearly equal to a perturber (correction functions).[70] The problem was reduced by adding an imaginary shift correction (0.1)[71] in the calculations. Another issue concerns the unbalanced description of the zeroth-order Hamiltonian for the open- and closed-shell electronic configurations, which was attenuated by introducing an ionization-potential-electron-affinity shift value (IPEA, 0.25)[72] in the zero-order Hamiltonian.[73]

NEVPT2 implements a second order perturbation theory to the CAS-type full configuration interaction (CAS-CI) wavefunction.[44,74] NEVPT2 does not have intruder state,[75] neither does it require level-shift correction or IPEA.[76] But NEVPT2 calculations were much time-demanding. On the basis of a compromise between computational cost and accuracy, the 6-31+G(d,p) basis set was adopted for the NEVPT2 calculations, and the active space was set

to (15e,12o) which includes (8e,6o) of $^1O_2$ and (7e,6o) of nucleobase.

In this work, the CASPT2- and NEVPT2-calculated reaction enthalpies included the 298 K thermal corrections that were calculated at the ωB97XD/6-31 + G(d,p) level. As a calibration, we calculated the $^1O_2$ excitation energy using AP-ωB97XD/6-31 + G(d,p), CASPT2(12,8)/6-31G(d,p) and NEVPT2(8,6)/6-31 + G(d,p). The energy is 1.02 eV at AP-ωB97XD, 1.05 eV at CASPT2, and 0.91 eV at NEVPT2. For comparison, the experimental $^1O_2$ excitation energy is 0.98 eV.[59a] Furthermore, in our previous study on the $^1O_2$ reactions with monohydrated 9-methylguanine radical cation[46] and monohydrated 9-methylguanine−1-methylcytosine base-pair radical cation,[41c] the CASPT2 method was able to quantitatively reproduce their experimentally measured reaction exothermicity.

Supporting Information Summary

The IP and $E°$ of DNA components, reaction schemes and energies, coordinates for reaction structures. The authors have cited additional reference within the Supporting Information (Ref. [77–82]).

Acknowledgements

This work was supported by the National Science Foundation (grant no. CHE 1856362). M. M. M. acknowledges the CUNY Graduate Center Mina Rees Dissertation Fellowship. We are grateful to Professor Bernhard Lippert (University of Dortmund, Germany) for providing us 9MOG.

Conflict of Interests

The authors declare no conflict of interest.

Data Availability Statement

The data that support the findings of this study are available in the supplementary material of this article.

Keywords: guided-ion beam tandem mass spectrometry · intra-base pair proton transfer · 9-methyl-8-oxoguanine−1-methylcytosine base-pair radical cation · non-statistical base-pair dissociation kinetics · singlet oxygen

[1] J. E. Klaunig, L. M. Kamendulis, *Annu. Rev. Pharmacol.* **2004**, *44*, 239–267.
[2] a) J. Zhou, O. Kostko, C. Nicolas, X. Tang, L. Belau, M. S. De Vries, M. Ahmed, *J. Phys. Chem. A* **2009**, *113*, 4829–4832; b) M. Schwell, M. Hochlaf, *Top. Curr. Chem.* **2015**, *355*, 155–208.
[3] C. E. Crespo-Hernández, R. Arce, Y. Ishikawa, L. Gorb, J. Leszczynski, D. M. Close, *J. Phys. Chem. A* **2004**, *108*, 6373–6377.
[4] S. Steenken, S. V. Jovanovic, *J. Am. Chem. Soc.* **1997**, *119*, 617–618.
[5] a) T. Douki, J. Cadet, *Int. J. Radiat. Biol.* **1999**, *75*, 571–581; b) T. Douki, S. Spinelli, J.-L. Ravanat, J. Cadet, *J. Chem. Soc., Perkin Trans. 2* **1999**, 1875–1880; c) G. Pratviel, B. Meunier, *Chem. Eur. J.* **2006**, *12*, 6018–6030; d) J. Cadet, T. Douki, J.-L. Ravanat, *Acc. Chem. Res.* **2008**, *41*, 1075–1083; e) J. Cadet, T. Douki, J.-L. Ravanat, *Free Radic. Biol. Med.* **2010**, *49*, 9–21; f) J. Cadet, J. R. Wagner, *Cold Spring Harbor Perspect. Biol.* **2013**, *5*, A012559; g) J. Cadet, J. R. Wagner, *Arch. Biochem. Biophys.* **2014**, *557*, 47–54; h) A. M. Fleming, C. J. Burrows, *Free Radic. Biol. Med.* **2017**, *107*, 35–52.
[6] C. Sheu, C. S. Foote, *J. Am. Chem. Soc.* **1993**, *115*, 10446–10447.
[7] P. R. Ogilby, *Chem. Soc. Rev.* **2010**, *39*, 3181–3209.
[8] J. Cadet, T. Douki, D. Gasparutto, J.-L. Ravanat, *Mutation Res.* **2003**, *531*, 5–23.
[9] S. Raoul, M. Berger, G. W. Buchko, P. C. Joshi, B. Morin, M. Weinfeld, J. Cadet, *J. Chem. Soc., Perkin Trans. 2* **1996**, 371–381.
[10] J. Cadet, M. Berger, G. W. Buchko, P. C. Joshi, S. Raoul, J.-L. Ravanat, *J. Am. Chem. Soc.* **1994**, *116*, 7403–7404.
[11] S. Steenken, *Chem. Rev.* **1989**, *89*, 503–520.
[12] a) J. Cadet, J.-L. Ravanat, G. R. Martinez, M. H. G. Medeiros, P. Di Mascio, *Photochem. Photobiol.* **2006**, *82*, 1219–1225; b) A. M. Fleming, C. J. Burrows, *DNA Repair* **2017**, *56*, 75–83.
[13] J.-L. Ravanat, G. R. Martinez, M. H. G. Medeiros, P. Di Mascio, J. Cadet, *Tetrahedron* **2006**, *62*, 10709–10715.
[14] a) Y. Ye, J. G. Muller, W. Luo, C. L. Mayne, A. J. Shallop, R. A. Jones, C. J. Burrows, *J. Am. Chem. Soc.* **2003**, *125*, 13926–13927; b) G. R. Martinez, J.-L. Ravanat, J. Cadet, M. H. Gennari de Medeiros, P. Di Mascio, *J. Mass Spectrom.* **2007**, *42*, 1326–1332; c) Y. Ye, J. G. Muller, C. J. Burrows, *J. Org. Chem.* **2006**, *71*, 2181–2184.
[15] F. Prat, K. N. Houk, C. S. Foote, *J. Am. Chem. Soc.* **1998**, *120*, 845–846.
[16] a) S. Steenken, S. V. Jovanovic, M. Bietti, K. Bernhard, *J. Am. Chem. Soc.* **2000**, *122*, 2373–2374; b) S. Wei, Z. Zhang, S. Liu, and Y. Wang, *New J. Chem.* **2021**, *45*, 11202–11212.
[17] a) C. Sheu, C. S. Foote, *J. Am. Chem. Soc.* **1995**, *117*, 6439–6442; b) G. R. Martinez, M. H. G. Medeiros, J.-L. Ravanat, J. Cadet, P. Di Mascio, *Biol. Chem.* **2002**, *383*, 607–617.
[18] a) C. Sheu, C. S. Foote, *J. Am. Chem. Soc.* **1995**, *117*, 474–477; b) G. W. Buchko, J. R. Wagner, J. Cadet, S. Raoul, M. Weinfeld, *Biochim. Biophys. Acta, Gene Struct. Expression* **1995**, *1263*, 17–24; c) S. Raoul, J. Cadet, *J. Am. Chem. Soc.* **1996**, *118*, 1892–1898; d) R. P. Hickerson, F. Prat, J. G. Muller, C. S. Foote, C. J. Burrows, *J. Am. Chem. Soc.* **1999**, *121*, 9423–9428; e) V. Duarte, J. G. Muller, C. J. Burrows, *Nucleic Acids Res.* **1999**, *27*, 496–502; f) V. Duarte, D. Gasparutto, L. F. Yamaguchi, J.-L. Ravanat, G. R. Martinez, M. H. G. Medeiros, P. Di Mascio, J. Cadet, *J. Am. Chem. Soc.* **2000**, *122*, 12622–12628; g) V. Duarte, D. Gasparutto, M. Jaquinod, J.-L. Ravanat, J. Cadet, *Chem. Res. Toxicol.* **2001**, *14*, 46–53; h) J. E. B. McCallum, C. Y. Kuniyoshi, C. S. Foote, *J. Am. Chem. Soc.* **2004**, *126*, 16777–16782; i) B. Matter, D. Malejka-Giganti, A. S. Csallany, N. Tretyakova, *Nucleic Acids Res.* **2006**, *34*, 5449–5460; j) B. H. Munk, C. J. Burrows, H. B. Schlegel, *J. Am. Chem. Soc.* **2008**, *130*, 5245–5256; k) Y. Sun, W. Lu, J. Liu, *J. Phys. Chem. B* **2017**, *121*, 956–966; l) M. M. Moe, M. Tsai, J. Liu, *ChemPlusChem* **2021**, *86*, 1243–1254; m) J.-L. Ravanat, E. Dumont, *Photochem. Photobiol.* **2022**, *98*, 564–571.
[19] L. A. Lipscomb, M. E. Peek, M. L. Morningstar, S. M. Verghis, E. M. Miller, A. Rich, J. M. Essigmann, L. D. Williams, *PNAS* **1995**, *92*, 719–723.
[20] Y. Oda, S. Uesugi, M. Ikehara, S. Nishimura, Y. Kawase, H. Ishikawa, H. Inoue, E. Ohtsuka, *Nucleic Acids Res.* **1991**, *19*, 1407–1412.
[21] J. A. Dean, *Lange's Handbook of Chemistry*, 15th ed., McGraw-Hill, New York, **1999**, p8.27.
[22] A. M. Fleming, J. G. Muller, A. C. Dlouhy, C. J. Burrows, *J. Am. Chem. Soc.* **2012**, *134*, 15091–15102.
[23] J. Reynisson, S. Steenken, *J. Mol. Struct.: Theochem* **2005**, *723*, 29–36.
[24] B. L. Westcott, N. E. Gruhn, L. J. Michelsen, D. L. Lichtenberger, *J. Am. Chem. Soc.* **2000**, *122*, 8083–8084.
[25] A. Kumar, M. D. Sevilla, *J. Phys. Chem. B* **2014**, *118*, 5453–5458.
[26] Y. Sun, M. M. Moe, J. Liu, *Phys. Chem. Chem. Phys.* **2020**, *22*, 14875–14888.
[27] Y. Fang, J. Liu, *J. Phys. Chem. A* **2009**, *113*, 11250–11261.
[28] a) C. Rebick, R. D. Levine, *J. Chem. Phys.* **1973**, *58*, 3942–3952; b) R. D. Levine, R. B. Bernstein, *Molecular Reaction Dynamics and Chemical Reactivity*, Oxford University Press, New York, **1987**; c) P. B. Armentrout, *Int. J. Mass Spectrom.* **2000**, *200*, 219–241; d) J. Liu, B. van Devener, S. L. Anderson, *J. Chem. Phys.* **2002**, *116*, 5530–5543.
[29] W. Zhou, J. Liu, S. D. Chambreau, G. L. Vaghjiani, *Phys. Chem. Chem. Phys.* **2022**, *24*, 14033–14043.
[30] a) C. Larriba, C. J. Hogan Jr., *J. Comput. Phys.* **2013**, *251*, 344–363; b) C. Larriba-Andaluz, C. J. Hogan Jr., *J. Chem. Phys.* **2014**, *141*, 194107.
[31] R. A. Marcus, *J. Chem. Phys.* **1952**, *20*, 359–364.
[32] T. Baer, W. L. Hase, *Unimolecular reaction dynamics: Theory and experiments*, Oxford University Press, New York, **1996**.

[33] a) M. T. Rodgers, K. M. Ervin, P. B. Armentrout, *J. Chem. Phys.* **1997**, *106*, 4499–4508; b) F. Meyer, F. A. Khan, P. B. Armentrout, *J. Am. Chem. Soc.* **1995**, *117*, 9740–9748; c) M. B. More, E. D. Glendening, D. Ray, D. Feller, P. B. Armentrout, *J. Phys. Chem.* **1996**, *100*, 1605–1614; d) D. Ray, D. Feller, M. B. More, E. D. Glendening, P. B. Armentrout, *J. Phys. Chem.* **1996**, *100*, 16116–16125; e) M. T. Rodgers, P. B. Armentrout, *J. Chem. Phys.* **1998**, *109*, 1787–1800.
[34] W. Lu, J. Liu, *Phys. Chem. Chem. Phys.* **2016**, *18*, 32222–32237.
[35] Y. Sun, M. M. Moe, J. Liu, *Phys. Chem. Chem. Phys.* **2020**, *22*, 24986–25000.
[36] M. M. Moe, J. Benny, J. Liu, *Phys. Chem. Chem. Phys.* **2022**, *24*, 9263–9276.
[37] M. M. Moe, J. Benny, Y. Sun, J. Liu, *Phys. Chem. Chem. Phys.* **2021**, *23*, 9365–9380.
[38] J. Troe, *Chem. Phys. Lett.* **1985**, *122*, 425–430.
[39] A. Maranzana, G. Ghigo, G. Tonachini, *J. Am. Chem. Soc.* **2000**, *122*, 1414–1423.
[40] a) T. J. Lee, P. R. Taylor, *Int. J. Quantum Chem., Quantum Chem. Symp.* **1989**, *36*, 199–207; b) D. Jayatilaka, T. J. Lee, *J. Chem. Phys.* **1993**, *98*, 9734–9747.
[41] a) K. Yamaguchi, F. Jensen, A. Dorigo, K. N. Houk, *Chem. Phys. Lett.* **1988**, *149*, 537–542; b) J. Benny, T. Saito, M. M. Moe, J. Liu, *J. Phys. Chem. A* **2022**, *126*, 68–79; c) M. M. Moe, T. Saito, M. Tsai, J. Liu, *J. Phys. Chem. B* **2022**, *126*, 5458–5472.
[42] a) K. Andersson, P. A. Malmqvist, B. O. Roos, *J. Chem. Phys.* **1992**, *96*, 1218–1226; b) M. Abe, G. Gopakmar, T. Nakajima, K. Hirao, in *Radiation Induced Molecular Phenomena in Nucleic Acids* (Eds.: K. Shukla, M. K., J. Leszczynski), Springer, Netherlands, **2008**, pp. 157–177.
[43] B. O. Roos, P. R. Taylor, E. M. Siegbahn, *Chem. Phys.* **1980**, *48*, 157–173.
[44] a) C. Angeli, R. Cimiraglia, S. Evangelisti, T. Leininger, J.-P. Malrieu, *J. Chem. Phys.* **2001**, *114*, 10252–10264; b) C. Angeli, R. Cimiraglia, J.-P. Malrieu, *J. Chem. Phys.* **2002**, *117*, 9138–9153.
[45] B. Thapa, B. H. Munk, C. J. Burrows, H. B. Schlegel, *Chem. Eur. J.* **2017**, *23*, 5804–5813.
[46] Y. Sun, M. Tsai, M. M. Moe, J. Liu, *J. Phys. Chem. A* **2021**, *125*, 1564–1576.
[47] a) K. E. McAuley-Hecht, G. A. Leonard, N. J. Gibson, J. B. Thomson, W. P. Watson, W. N. Hunter, T. Brown, *Biochem.* **1994**, *33*, 10266–10270; b) S. S. David, S. D. Williams, *Chem. Rev.* **1998**, *98*, 1221–1262; c) S. S. David, V. L. O'Shea, S. Kundu, *Nature* **2007**, *447*, 941–950.
[48] a) P. T. Henderson, J. C. Delaney, J. G. Muller, W. L. Neeley, S. R. Tannenbaum, C. J. Burrows, J. M. Essigmann, *Biochemistry* **2003**, *42*, 9257–9262; b) W. L. Neeley, J. M. Essigmann, *Chem. Res. Toxicol.* **2006**, *19*, 491–505.
[49] R. K. O. Sigel, E. Freisinger, B. Lippert, *JBIC, J. Biol. Inorg. Chem.* **2000**, *5*, 287–299.
[50] a) S. Wee, R. A. J. O'Hair, W. D. McFadyen, *Rapid Commun. Mass Spectrom.* **2005**, *19*, 1797–1805; b) A. K. Y. Lam, B. F. Abrahams, M. J. Grannas, W. D. McFadyen, R. A. J. O'Hair, *Dalton Trans.* **2006**, 5051–5061.
[51] P. Cheng, D. K. Bohme, *J. Phys. Chem. B* **2007**, *111*, 11075–11082.
[52] a) L. Feketeová, E. Yuriev, J. D. Orbell, G. N. Khairallah, R. A. J. O'Hair, *Int. J. Mass Spectrom.* **2011**, *304*, 74–82; b) L. Feketeová, B. Chan, G. N. Khairallah, V. Steinmetz, P. Maitre, L. Radom, R. A. J. O'Hair, *J. Phys. Chem. Lett.* **2017**, *8*, 3159–3165.
[53] K. M. Ervin, P. B. Armentrout, *J. Chem. Phys.* **1985**, *83*, 166–189.
[54] P. B. Armentrout, *J. Anal. At. Spectrom.* **2004**, *19*, 571–580.
[55] J. Liu, K. Song, W. L. Hase, S. L. Anderson, *J. Chem. Phys.* **2003**, *119*, 3040–3050.
[56] H. Koizumi, P. B. Armentrout, *J. Chem. Phys.* **2003**, *119*, 12819–12829.
[57] M. B. Sowa-Resat, P. A. Hintz, S. L. Anderson, *J. Phys. Chem.* **1995**, *99*, 10736–10741.
[58] a) A. Midey, I. Dotan, A. A. Viggiano, *J. Phys. Chem. A* **2008**, *112*, 3040–3045; b) A. A. Viggiano, A. Midey, N. Eyet, V. M. Bierbaum, J. Troe, *J. Chem. Phys.* **2009**, *131*, 094303; c) Y. Fang, F. Liu, A. Bennett, S. Ara, J. Liu, *J. Phys. Chem. B* **2011**, *115*, 2671–2682.
[59] a) W. J. Lafferty, A. M. Solodov, C. L. Lugez, G. T. Fraser, *Appl. Opt.* **1998**, *37*, 2264–2270; b) S. M. Newman, I. C. Lane, A. J. Orr-Ewing, D. A. Newnham, J. Ballard, *J. Chem. Phys.* **1999**, *110*, 10749–10757.
[60] M. Al-Sheikhly, *Radiat. Phys. Chem.* **1994**, *44*, 297–301.
[61] F. B. van Duijneveldt, J. G. C. M. van Duijneveldt-van de Rijdt, J. H. van Lenthe, *Chem. Rev.* **1994**, *94*, 1873–1885.
[62] Gaussian 16 (Revision D.01)M. J. Frisch, G. W. Trucks, H. B. Schlegel, G. E. Scuseria, M. A. Robb, J. R. Cheeseman, G. Scalmani, V. Barone, G. A. Petersson, H. Nakatsuji, X. Li, M. Caricato, A. V. Marenich, J. Bloino, B. G. Janesko, R. Gomperts, B. Mennucci, H. P. Hratchian, J. V. Ortiz, A. F. Izmaylov, J. L. Sonnenberg, D. Williams-Young, F. Ding, F. Lipparini, F. Egidi, J. Goings, B. Peng, A. Petrone, T. Henderson, D. Ranasinghe, V. G. Zakrzewski, J. Gao, N. Rega, G. Zheng, W. Liang, M. Hada, M. Ehara, K. Toyota, R. Fukuda, J. Hasegawa, M. Ishida, T. Nakajima, Y. Honda, O. Kitao, H. Nakai, T. Vreven, K. Throssell, J. A. Montgomery Jr., J. E. Peralta, F. Ogliaro, M. J. Bearpark, J. J. Heyd, E. N. Brothers, K. N. Kudin, V. N. Staroverov, T. A. Keith, R. Kobayashi, J. Normand, K. Raghavachari, A. P. Rendell, J. C. Burant, S. S. Iyengar, J. Tomasi, M. Cossi, J. M. Millam, M. Klene, C. Adamo, R. Cammi, J. W. Ochterski, R. L. Martin, K. Morokuma, O. Farkas, J. B. Foresman, D. J. Fox, Gaussian, Inc., Wallingford, CT, **2016**.
[63] D. G. Liakos, M. Sparta, M. K. Kesharwani, J. M. L. Martin, F. Neese, *J. Chem. Theory Comput.* **2015**, *11*, 1525–1539.
[64] K. Raghavachari, G. W. Trucks, J. A. Pople, M. Head-Gordon, *Chem. Phys. Lett.* **1989**, *157*, 479–483.
[65] F. Neese, *WIREs Comput. Mol. Sci.* **2018**, *8*, e1327.
[66] I. M. Alecu, J. Zheng, Y. Zhao, D. G. Truhlar, *J. Chem. Theory Comput.* **2010**, *6*, 2872–2887.
[67] L. Zhu and W. L. Hase *A general RRKM program (QCPE 644), Quantum Chemistry Program Exchange*, Chemistry Department, University of Indiana: Bloomington (1993).
[68] T. Beyer, D. F. Swinehart, *Commun. ACM* **1973**, *16*, 379.
[69] a) I. Fdez. Galván, M. Vacher, A. Alavi, C. Angeli, F. Aquilante, J. Autschbach, J. J. Bao, S. I. Bokarev, N. A. Bogdanov, R. K. Carlson, L. F. Chibotaru, J. Creutzberg, N. Dattani, M. G. Delcey, S. S. Dong, A. Dreuw, L. Freitag, L. M. Frutos, L. Gagliardi, F. Gendron, A. Giussani, L. González, G. Grell, M. Guo, C. E. Hoyer, M. Johansson, S. Keller, S. Knecht, G. Kovačević, E. Källman, G. Li Manni, M. Lundberg, Y. Ma, S. Mai, J. P. Malhado, P. Å. Malmqvist, P. Marquetand, S. A. Mewes, J. Norell, M. Olivucci, M. Oppel, Q. M. Phung, K. Pierloot, F. Plasser, M. Reiher, A. M. Sand, I. Schapiro, P. Sharma, C. J. Stein, L. K. Sørensen, D. G. Truhlar, M. Ugandi, L. Ungur, A. Valentini, S. Vancoillie, V. Veryazov, O. Weser, T. A. Wesołowski, P.-O. Widmark, S. Wouters, A. Zech, J. P. Zobel, R. Lindh, *J. Chem. Theory Comput.* **2019**, *15*, 5925–5964; b) F. Aquilante, J. Autschbach, A. Baiardi, S. Battaglia, V. A. Borin, L. F. Chibotaru, I. Conti, L. D. Vico, M. Delcey, I. F. Galván, N. Ferré, L. Freitag, M. Garavelli, X. Gong, S. Knecht, E. D. Larsson, R. Lindh, M. Lundberg, P. Å. Malmqvist, A. Nenov, J. Norell, M. Odelius, M. Olivucci, T. B. Pedersen, L. Pedraza-González, Q. M. Phung, K. Pierloot, M. Reiher, I. Schapiro, J. Segarra-Martí, F. Segatta, L. Seijo, S. Sen, D.-C. Sergentu, C. J. Stein, L. Ungur, M. Vacher, A. Valentini, V. Veryazov, *J. Chem. Phys.* **2020**, *152*, 214117.
[70] B. O. Roos, K. Andersson, *Chem. Phys. Lett.* **1995**, *245*, 215–223.
[71] N. Forsberg, P.-Å. Malmqvist, *Chem. Phys. Lett.* **1997**, *274*, 196–204.
[72] D. Roca-Sanjuán, M. Rubio, M. Merchán, L. Serrano-Andrés, *J. Chem. Phys.* **2006**, *125*, 084302.
[73] G. Ghigo, B. O. Roos, P.-A. Malmqvist, *Chem. Phys. Lett.* **2004**, *396*, 142–149.
[74] B. G. Levine, A. S. Durden, M. P. Esch, F. Liang, Y. Shu, *J. Chem. Phys.* **2021**, *154*.
[75] R. Cimiraglia, C. Angeli, *AIP Conference Proceedings* **2007**, *963*, 599–602.
[76] R. Sarkar, P.-F. Loos, M. Boggio-Pasqua, D. Jacquemin, *J. Chem. Theor. Comput.* **2022**, *18*, 2418–2436.
[77] C. J. Burrows, J. G. Muller, *Chem. Rev.* **1998**, *98*, 1109–1151.
[78] D. Touboul, F. Gaie-Levrel, G. A. Garcia, L. Nahon, L. Poisson, M. Schwell, M. Hochlaf, *J. Chem. Phys.* **2013**, *138*, 094203.
[79] H.-W. Jochims, M. Schwell, H. Baumgaertel, S. Leach, *Chem. Phys.* **2005**, *314*, 263–282.
[80] a) E. Pluhařová, M. Ončák, R. Seidel, C. Schroeder, W. Schroeder, B. Winter, S. E. Bradforth, P. Jungwirth, P. Slavíček, *J. Phys. Chem. B* **2012**, *116*, 13254–13264; b) C. A. Schroeder, E. Pluharova, R. Seidel, W. P. Schroeder, M. Faubel, P. Slavicek, B. Winter, P. Jungwirth, S. E. Bradforth, *J. Am. Chem. Soc.* **2015**, *137*, 201–209.
[81] X.-B. Wang, E. R. Vorpagel, X. Yang, L.-S. Wang, *J. Phys. Chem. A* **2001**, *105*, 10468–10474.
[82] L. P. Candeias, S. Steenken, *J. Am. Chem. Soc.* **1992**, *114*, 699–704.

Manuscript received: July 21, 2023
Revised manuscript received: September 18, 2023
Accepted manuscript online: September 22, 2023
Version of record online: September 22, 2023

RESEARCH ARTICLE

Intra-base pair proton transfer enhances the oxidizability of the 8-oxoguanine radical within a Watson–Crick 8-oxoguanine–cytosine base-pair radical cation, and the proton transfer also leads to non-statistical base-pair dissociation upon collisional activation.

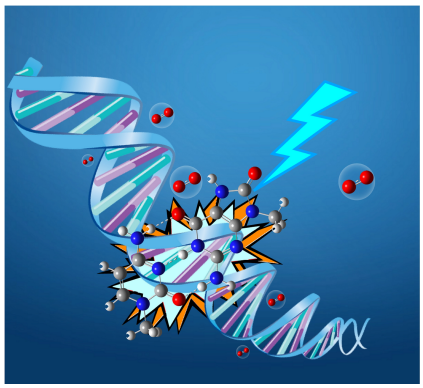

*M. M. Moe, Prof. Dr. M. Tsai, Prof. Dr. J. Liu**